Gondwana Research 133 (2024) 297–322

Contents lists available at ScienceDirect

Gondwana Research

journal homepage: www.elsevier.com/locate/gr

What controls structural variations along the Zagros Collision Zone? Insights from geophysical observations and thermo-mechanical modelling

Magdala Tesauro [a,b,*], Petra Maierová [c], Alexander Koptev [d], Alberto Pastorutti [a], Tommaso Pivetta [a,e], Ivan Koulakov [f,g], Carla Braitenberg [a]

[a] Department of Mathematics, Informatics and Geosciences, University of Trieste, Trieste, Italy
[b] University of Utrecht, Department of Geosciences, the Netherlands
[c] Czech Geological Survey, Klárov 3/131, 118 00 Prague 1, Czech Republic
[d] GFZ German Research Centre for Geosciences, Potsdam, Germany
[e] Istituto Nazionale di Geofisica e Vulcanologia, Sezione di Napoli–Osservatorio Vesuviano, Naples, Italy
[f] Trofimuk Institute of Petroleum Geology and Geophysics, SB RAS, Prospekt Koptyuga, Novosibirsk, Russia
[g] Novosibirsk State University, Novosibirsk, Russia

ARTICLE INFO

Article history:
Received 6 August 2023
Revised 28 February 2024
Accepted 14 June 2024
Available online 20 June 2024
Handling Editor: Taras Gerya

Keywords:
Zagros orogen
Geophysical data
Crustal relamination
Thermo-mechanical modelling
Oblique collision
Forward gravity models

ABSTRACT

The Zagros Collision Zone is a complex tectonic region formed as a consequence of the collision between Arabia and Eurasia after the subduction of the Neo-Tethys ocean. The NW-SE striking Zagros orogen consists of the following parallel tectonic units (from SW to NE): Zagros Fold and Thrust Belt (ZFTB), Sanandaj–Sirjan Metamorphic Zone (SSZ), and Urumieh–Dokhtar Magmatic Arc (UDMA). In this study, we perform a combined analysis of recent geophysical data, revealing pronounced differences in the crustal and lithospheric structure along the Zagros Mountains. The northwestern sector shows a fairly uniform crustal thickening across the broad symmetric orogen from the ZFTB to the UDMA. In contrast, in the central Zagros, the transition from a relatively narrow zone of high elevations and high-frequency relief in the ZFTB to a smoother surface topography of the SSZ and UDMA occurs with an abrupt increase in Moho depth below the SSZ. The last observation has recently been interpreted as a result of "relamination" process, where the felsic upper crust of the Arabian plate underthrust the mafic crust of the Iranian plate. We present geodynamic numerical models of crustal relamination during continental collision and compute static gravity field of the resulting structures. We show that oblique closure of the Neo-Tethys affects lateral variations in the style and extent of crustal relamination, which control the observed along-strike changes in crustal configuration and orogen altitude. In particular, a narrow and higher orogen (as in the central Zagros) develops in the experiments with a young and wide oceanic plate, whereas an old and narrow subducting plate tends to form a broad and lower topography (as in the northwestern Zagros). This is geometrically consistent with the progressive closure of the Neo-Tethys from NW to SE during the oblique continental collision between Arabia and Eurasia.

1. Introduction

The continental collision between the Arabian plate and the southern Eurasian margin resulted in the formation of the Zagros Collision Zone, which extends in NW-SE direction for nearly 2000 km. Although both the crust and the upper mantle of the Zagros orogen have been investigated by numerous geological and geophysical studies over the past 50 years, the geometry and physical state of its structures, that accommodate the internal deformation caused by past and present convergence, are still controversial (e.g., Paul et al., 2006, 2010; Agard et al., 2011; Ballato et al., 2011; Kaviani et al., 2020; Boutoux et al., 2021; Irandoust et al., 2022). The diachroneity of the collision process, that was gradually expanded from eastern Turkey to southeastern Iran (Darin and Umhoefer, 2022), is probably the main reason for the complexity of the lithospheric architecture, seismicity distribution, and topography, which are subject to pronounced variations not

* Corresponding author.
E-mail address: mtesauro@units.it (M. Tesauro).

https://doi.org/10.1016/j.gr.2024.06.009
1342-937X/

only across (from SW to NE) but also along (from NW to SE) the collision zone (e.g., Kaviani et al., 2020; Talebi et al., 2020; Irandoust et al., 2022; Yang et al., 2023a), as also more recently evidenced in a density and magnetic susceptibility model, obtained by the joint inversion of gravity and magnetic data (Maurizio et al., 2023).

Recently, the crustal structure in the central section of the Zagros has been interpreted as a product of the "relamination" process, in which the felsic upper crust of the Arabian plate underthrusts the high-seismic-velocity mafic crust of the Iranian plate (Talebi et al., 2020). As opposed to "delamination" (Bird, 1979; Ueda et al., 2012), the term "relamination" (Hacker et al., 2011; Maierová et al., 2018) refers to the detachment of crustal material from the subducting plate and its emplacement at the base ("sublithospheric relamination") or within the overriding plate ("crustal relamination"). The large thickness of the crust detected by seismological studies in the Zagros orogen (Kaviani et al., 2020; Irandoust et al., 2022) can, therefore, potentially be attributed to a second type of relamination ("crustal relamination").

In this study, we examine the available geophysical data on the Zagros Collision Zone with a particular focus on along-strike (orogen-parallel) variations and a possible link to the relamination process. Specifically, we use (1) seismic tomography models of the crust (Kaviani et al., 2020; Irandoust et al., 2022) and upper mantle (Koulakov, 2011; Schaeffer and Lebedev, 2013; Veisi et al., 2021), (2) Moho depth obtained from shear wave models (Kaviani et al., 2020; Irandoust et al., 2022), (3) seismicity distribution from the most updated seismic database (NEIC catalogue, https://earthquake.usgs.gov/earthquakes/search), (4) Curie point depth derived from magnetic anomaly inversion (Li et al., 2017), and (5) Bouguer anomalies based on the global gravity model XGM2019e (Zingerle et al., 2020). The revealed architecture of the crust and lithospheric mantle was visually compared with across-strike and along-strike variations in surface topography (ETOPO 1, Amante and Eakins, 2009). In addition, we provide a quantitative assessment of the statistical correlation between surface topography (Amante and Eakins, 2009), Moho depth (Kaviani et al., 2020; Irandoust et al., 2022), and Bouguer gravity anomalies (Zingerle et al., 2020).

To explore the mechanism of *syn*-collisional crustal relamination, we perform a series of two-dimensional (2D) thermo-mechanical experiments built on several previous numerical studies that have investigated this process to explain fundamental features of ancient and modern orogens, such as the European Variscides and the Himalayan-Tibetan system (Sizova et al., 2012; Labrousse et al., 2015; Liu et al., 2017; Maierová et al., 2018; Schliffke et al., 2019). We test different control parameters to capture the heterogeneity of the colliding plates and obliquity of the continental collision and to understand their influence on along-strike differences in the present-day structure of the Zagros orogen. The modelling outcomes, such as the shape of the subducting slab, the configuration of the overriding-plate crust, and the topography, were compared with the available observations, i.e. with the seismic tomography and other geophysical data and the relief variations across the orogen in the different parts (northwestern and central) of the collision zone. Furthermore, the static gravity field of the structures determined in the thermo-mechanical experiments was computed and compared with the present-day gravity anomalies.

2. Tectonic setting and geodynamic history

The Zagros Collision Zone has been formed during the collision of the Arabian and Iranian plates. The Central and Eastern Iran is a relatively flat area, bordered to the north by the Turan Platform and to the east by the Afghan Block (Fig. 1), comprising several tectonic micro-blocks (from W to E: the Yazd, Tabas, and Lut blocks), collectively referred to as the CEIM (central-east Iranian micro-blocks). During the Permian, these micro-blocks were separated from Eurasia in the north by the Paleo-Tethys ocean and were detached from the eastern margin of Gondwana with the opening of the Neo-Tethys ocean in the south (Muttoni et al., 2009). In the Late Triassic, the CEIM was attached to the southern margin of stable Eurasia (Turan Platform), forming the Cimmerian orogen in Northern Iran (Wilmsen et al., 2009). The Paleo-Tethys suture is thought to be located in Northern Iran, where it extends along the Alborz-Binalud and Kopeh Dagh mountain ranges (Zanchi et al., 2009).

Subduction of the Neo-Tethys oceanic slab began during the Early to Middle Jurassic (Agard et al., 2011), likely as a consequence of the opening of the Central Atlantic Ocean (Sibuet et al., 2012). The back-arc extension triggered by the northward subduction of the Neo-Tethys has caused the collapse of the Cimmerian orogen with the formation of the post-Triassic sedimentary basin in the Kopeh Dagh and the opening of several small-scale and short-lived oceanic basins, surrounding the CEIM. Most of the Neo-Tethys was closed by the oblique collision between Arabia and Eurasia by ~ 30–10 Ma (Agard et al., 2011; Chiu et al., 2013), although subduction of the Neo-Tethys remnant in the Makran region is currently ongoing (Mc-Call, 1997).

The closure of the Neo-Tethys ocean along the Arabia-Eurasia margin and the associated continental collision led to the formation of the NW-SE striking Zagros orogen, which consists of several NW-SE trending tectonic provinces (Fig. 1): (1) the Zagros Fold and Thrust Belt (ZFTB); (2) the Sanandaj–Sirjan Metamorphic Zone (SSZ); and (3) the Urumieh–Dokhtar Magmatic Assemblage (UDMA). The ZFTB is the seismically active zone of the Zagros Mountains, separated from the SSZ by the Main Zagros Thrust (MZT), which is considered to be the boundary between the Arabian and Iranian plates. The SSZ is a highly deformed and moderately metamorphosed remnant of the southern active margin of the Iranian continental block. This tectonic unit consists of a ~150–200 km-wide belt of sedimentary and metamorphic Paleozoic to Mesozoic rocks intruded by Jurassic to Early Eocene calc-alkaline magmatic rocks and Middle Eocene gabbros (e.g., Agard et al., 2011). Geologic data indicate that magmatic activity in the SSZ nearly ceased during the Cretaceous and shifted toward the UDMA (e.g., Omrani et al., 2008). This magmatic shift was related to the flat-slab subduction that established in the Mid-Cretaceous (Verdel et al., 2011). The UDMA, characterized by almost continuous volcanic activity from the Eocene to the present, is an Andean-type volcanic arc, which is ~ 50–100 km-wide and composed of Late Jurassic to Quaternary magmatic rocks.

The main phases of deformation on the Arabian margin include ophiolite obduction in the Late Cretaceous-Eocene (e.g., Koshnaw et al., 2019; Vergés et al., 2019) and subsequent continental collision in the Late Eocene-Early Oligocene to Recent (e.g., Ballato et al., 2011; Darin and Umhoefer, 2022). Furthermore, thermochronological data, syntectonic sedimentation, and comparison between estimates of total shortening and extrapolated geodetic strain rates (e.g., Gavillot et al., 2010; Ballato et al., 2011; Madanipour et al., 2017; Barber et al., 2018; Vergés et al., 2019; Darin and Umhoefer, 2022) have shown that the collision phase can be subdivided into two stages separated by a time interval of ~15–20 Myr: the first stage without significant deformation (referred to as "soft collision") and the second stage, characterized by intense tectonic deformation, surface uplift, and rock exhumation (referred to as "hard collision"). Importantly, due to the irregular shape of the Arabian continental margin combined with the NNE direction of the Afro–Arabian plate motion relative to Eurasia, which led to oblique subduction of the Neo-Tethys, the continental collision along the Zagros orogen was strongly diachronous.

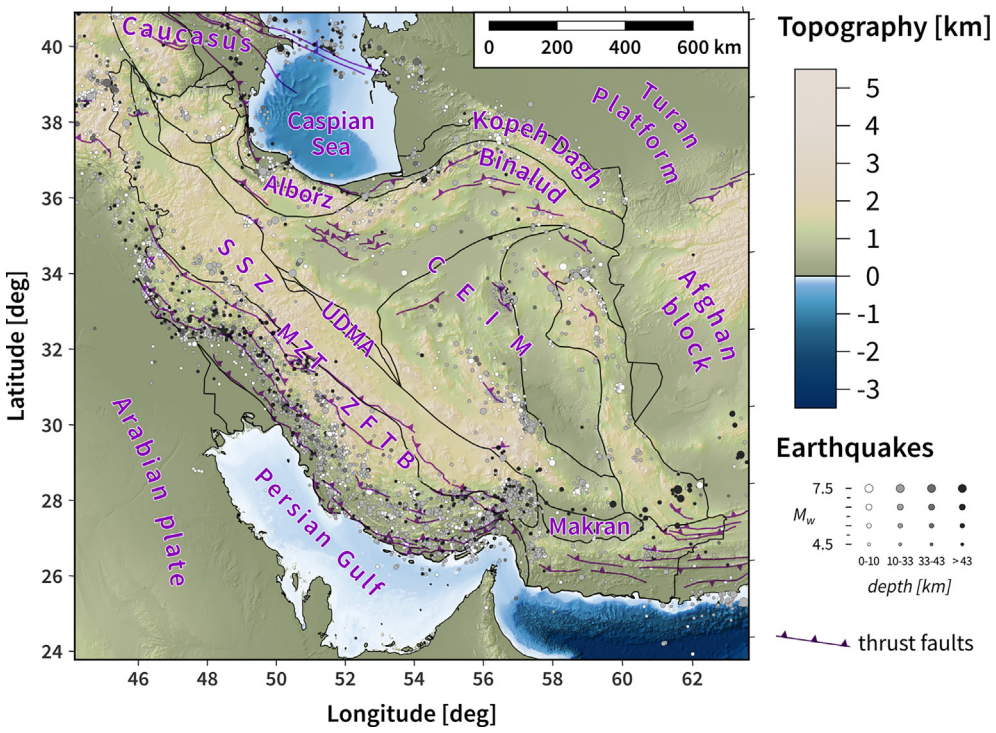

Fig. 1. Main tectonic units in the Iranian region of Arabia-Eurasia collision zone. Surface topography is from ETOPO 1 (Amante and Eakins, 2009) and thrust faults and tectonic blocks limits are from Rabiee et al. (2019). Circles with the radius proportional to the magnitude and fill color proportional to the depth show the earthquakes (NEIC catalogue, https://earthquake.usgs.gov/earthquakes/search), below and above the depth of 40 km, respectively. Abbreviations stand as follows: ZFTB, Zagros Fault and Thrust Belt; MZT, Main Zagros Thrust; SSZ, Sanandaj–Sirjan Metamorphic Zone; UDMA, Urumieh–Dokhtar Magmatic Arc, CEIM, Central-East Iranian Micro-blocks.

In particular, the onset of the collision initially took place in eastern Anatolia at ~42 Ma and then gradually shifted to the SE, occurring at ~40–35 Ma in northwestern Zagros, ~35–25 Ma in central Zagros, and ~25–15 Ma in southeastern Zagros (Darin and Umhoefer, 2022). This overall oblique convergence history led to a gradual transition from oceanic to continental subduction from NW to SE, which is also reflected in the geochemical signature of the magmatism, characterized by a diachronic transition from calc-alkaline, shoshonitic and adakitic rocks to predominantly high-K alkaline and minor sodic alkaline rocks (Rabiee et al., 2020).

The Cenozoic subduction of the Neo-Tethys ocean beneath the southern margin of Eurasia includes two slab break-off events. The first slab rupture occurred ~ 60–55 Ma during continuous oceanic subduction, while the second one happened in the Late Miocene as a result of continental collision (Agard et al., 2011). On the contrary, some geologic data, such as the adakitic magmas in the central part of the UDMA, presumably derived from the melting of the oceanic slab during its detachment (Omrani et al., 2008), and the recent transition from thin-skinned to thick-skinned deformation observed in the Zagros foreland (Molinaro et al., 2005), argue for a slab break-off in the Mio-Pliocene. In any case, the role of Neo-Tethys slab pull force in driving the movement of the Arabian plate has clearly diminished in the latest Cenozoic (Mouthereau et al., 2012), so that the convergence reduced from ~ 3–5 cm yr^{-1} (Boutoux et al., 2021) to the current rate of ~ 2.2 cm yr^{-1} (Khorrami et al., 2019; Vernant et al., 2004). The current convergence can be attributed to the combined effect of (1) the ridge push from the Gulf of Aden and the Red Sea spreading system (Molinaro et al., 2005); (2) the push of the Afar mantle plume (Koptev et al., 2018), which presumably triggers a large-scale asthenospheric flow below the Arabian plate (Ershov and Nikishin, 2004; Faccenna et al., 2013); and (3) the pull of the slab beneath Turkey, which remains connected to the Arabian plate (e.g., Mouthereau et al., 2012; Becker and Faccenna, 2011).

3. Main structures from geophysical data

3.1. Crustal seismic velocities

The crustal structure of the Zagros Collision Zone has been extensively studied in recent decades, mainly using receiver function analysis (e.g., Paul et al., 2006; Mohammadi et al., 2013; Wu et al., 2021) and seismic tomography (e.g., Kaviani et al., 2020; Veisi et al., 2021; Irandoust et al., 2022). The results revealed significant differences both in the Moho depth patterns and distribution of crustal velocities between the northwestern and central parts of the Zagros orogen. For example, analyses of receiver function data (Mohammadi et al., 2013; Motaghi et al., 2015, 2017; Paul et al., 2006, 2010) revealed crustal thicknesses of ~40–50 km under the entire external part of the chain (the ZFTB), with a sudden increase to a depth of ~60–70 km beneath the SSZ, in the central sector of the orogen and a thinning to ~50 km under the Alborz mountains and ~45 km beneath the Central Iran.

In the recent study of Kaviani et al. (2020), Rayleigh wave records from ambient-noise cross-correlations and regional earthquakes were used to construct a 3D model of shear wave velocity (v_s) for the crust and uppermost mantle (to a depth of 100 km) in this region (Fig. 2a). The results of this study show a relatively thin crust (~35–40 km) beneath the Arabian plate that rapidly thickens to ~ 45 km beneath the ZFTB deformation front (Fig. 2a). Consistent with previous studies, the Moho becomes progressively thicker (up to ~ 50 km) within a relatively narrow zone in the NE of the MZT. Further to the NE, the Moho shallows back to ~ 40 km beneath the Alborz mountains and to ~ 35 km beneath the Central Iran, which is thinner than previous estimates (e.g., Mohammadi et al., 2013). Under the Kopeh Dagh and Binalud mountains, the crust thickens again to ~ 45 km and then thins to ~ 30 km under the Turan Platform. In the southern part of the collision zone, beneath Makran, where the Neo-Tethys oceanic

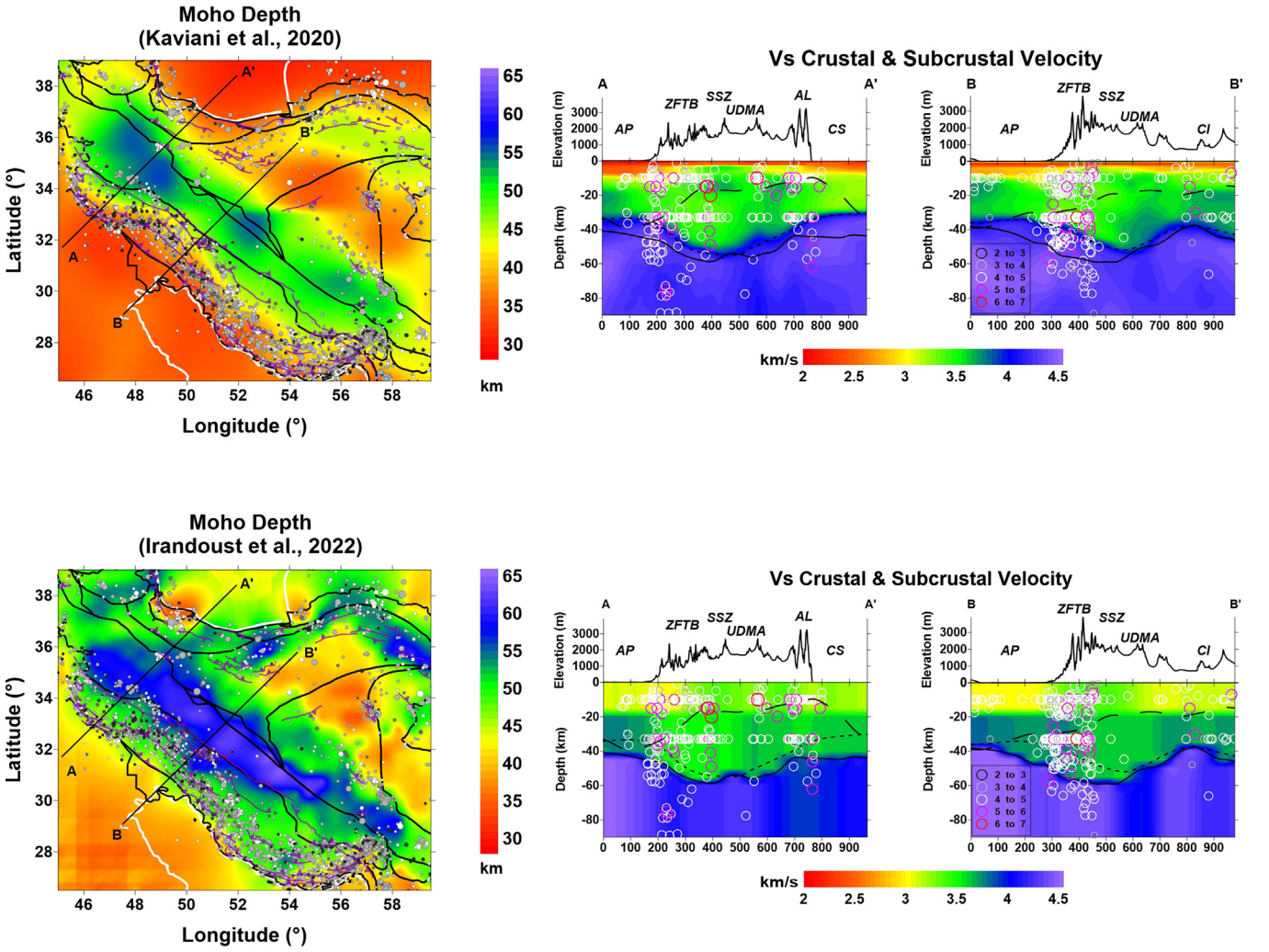

Fig. 2. Depth of Moho and shear wave velocities (v_s) illustrating crustal structure in the Zagros region, based on the analysis of Rayleigh wave records by (a) Kaviani et al. (2020) and (b) Irandoust et al. (2022). Shear wave velocities (v_s) are shown along two cross-sections (A-A' and B-B'), whose locations are marked on the Moho depth maps. Thrust faults and tectonic blocks limits on the maps are from Rabiee et al. (2019). Circles with the radius proportional to the magnitude and fill color proportional to the depth show the earthquakes (see Fig. 1 for the legend). Colored circles over the velocity cross-sections show the location of earthquakes of different magnitudes according to the legend. High-frequency dashed and solid lines on the cross-sections show the Moho depth of Kaviani et al. (2020) and Irandoust et al. (2022), while low-frequency dashed lines show the depth of the Curie temperature (Li et al., 2017), which is displayed in Fig. 3. Abbreviations stands as follows: AP, Arabian plate; ZFTB, Zagros Fault and Thrust Belt; SSZ, Sanandaj–Sirjan Metamorphic Zone; UDMA, Urumieh–Dokhtar Magmatic Arc; AL, Alborz mountains; CI, Central Iran; CS, Caspian Sea.

lithosphere is still subducting beneath the Eurasian plate, the Moho depth decreases to < 40 km (Fig. 2a).

Along the northwestern cross-section A-A', crustal thickening is quite uniform, with a maximum Moho depth of ~ 55 km, accompanied by a corresponding rise in surface topography up to ~ 2.5 km. Therefore, the northwestern part of the orogen has a fairly symmetric shape with a width of ~ 350 km, considering the lateral extent (from SW to NE) of the main tectonic units (the ZFTB, the SSZ, and the UDMA), composing the Zagros Collision Zone (Fig. 1). Further to the NE, below the Alborz mountains, the Moho depth decreases to ~ 35 km, while the surface topography increases to ~ 3 km. Along the central cross-section B-B', the Moho depth increases sharply, reaching its maximum of ~ 55 km beneath the inner part of the SSZ, while the topography decreases from ~ 3.5 km in the ZFTB to ~ 2 km in the SSZ and the UDMA, resulting in a decreasing width of the orogen, which in this case is strongly asymmetric. In both sections, low shear wave velocities (v_s < 3 km/s) down to depths of ~ 5–10 km are characteristic not only of the Arabian platform, where they correspond to the thick Phanerozoic sedimentary sequences, covering the underlying Precambrian basement, but also of the external part of the Zagros Collisional Zone (Fig. 2a). Moreover, the crust below the sediments composing the ZFTB also exhibits lower velocities than those of the adjacent tectonic units (the SSZ, the UDMA, the Central Iran, and the undeformed part of the Arabian platform). These velocity differences may be due to the fact that the units forming the southern margin of the Iranian plate (the SSZ and the UDMA) were volcanic arcs during the subduction of the Neo-Tethys ocean and, therefore, consist mainly of magmatic and metamorphic rocks with high seismic velocity and density. In contrast, there are no volcanic/metamorphic bodies in the ZFTB, which is mainly composed of accreted sediments that formed the Arabian continental margin before continental collision.

A more recent model of shear wave velocity (v_s) of Irandoust et al. (2022) shows a similar distribution of Moho depths to that of Kaviani et al. (2020), but with stronger lateral variations. Indeed, most of the Zagros orogen is characterized by a Moho depth of ~ 60 km, which rapidly decreases to ~ 45 km in the UDMA

and ~ 35 km in the Central Iran, and increases again to over ~ 55 km below the Kopeh Dagh and Binalud mountains (Fig. 2b). Moreover, the Moho beneath the Alborz mountains is also deeper (~50 km) than in Kaviani et al. (2020). Along cross-sections A-A' and B-B', the pattern of Moho depth is generally similar to that of Kaviani et al. (2020), but there are also some differences. In particular, the Moho of Irandoust et al. (2022) is systematically deeper by ~ 5–10 km along profile A-A', whereas its maximum is shifted by ~ 50 km to the SW from the inner to the central part of the SSZ along cross-section B-B' (compare Fig. 2a and b). Despite these discrepancies, the statistical correlation with the surface topography along both cross-sections remains relatively high for both models of Moho depth (within the interval of 0.67–0.89; Table 1). The distribution of shear velocity variations, which are given in the model of Irandoust et al. (2022) as averaged values for two crustal layers and the uppermost mantle, show lower values in the upper and lower crust beneath the ZFTB than in the surrounding areas (Fig. 2b), consistently with the results of the model of Kaviani et al. (2020).

As clearly shown by Kaviani et al. (2020), the crust of the overriding plate undergoes an abrupt thickening below the SSZ in the central part of the Zagros orogen (Fig. 2a). A detailed study by Talebi et al. (2020), based on the interpretation of P- and S-wave tomography, has revealed a complex crustal architecture in this segment of the collision zone that is not visible in the seismic velocity models of Kaviani et al. (2020) and Irandoust et al. (2022) discussed above. In particular, Talebi et al. (2020) demonstrate a vertical transition from a mafic layer with high seismic velocity to a low-velocity felsic layer, which in turn is underlain by another high-velocity mafic layer. Such a mafic-felsic-mafic alternation can be interpreted as the emplacement of the upper and lower crust of the Arabian plate, which have detached from the subducting mantle, beneath the exhumed mafic metamorphic complexes of the Iranian plate that currently form the uppermost part of the SSZ (see Fig. 3 in Talebi et al., 2020). This process of crustal relamination is favored by hot thermal conditions in the overriding plate (Maierová et al., 2018), which leads to ductile behavior of the mafic lower-crustal material and a consequent rheological decoupling of the upper crust from the lithospheric mantle (Koptev et al., 2019). According to this interpretation, the reduced and smooth surface topography observed in the SSZ and the UDMA along cross-section B-B' (Fig. 2) is the result of a predominantly ductile deformation regime in the warm and thin overriding plate (Talebi et al., 2020).

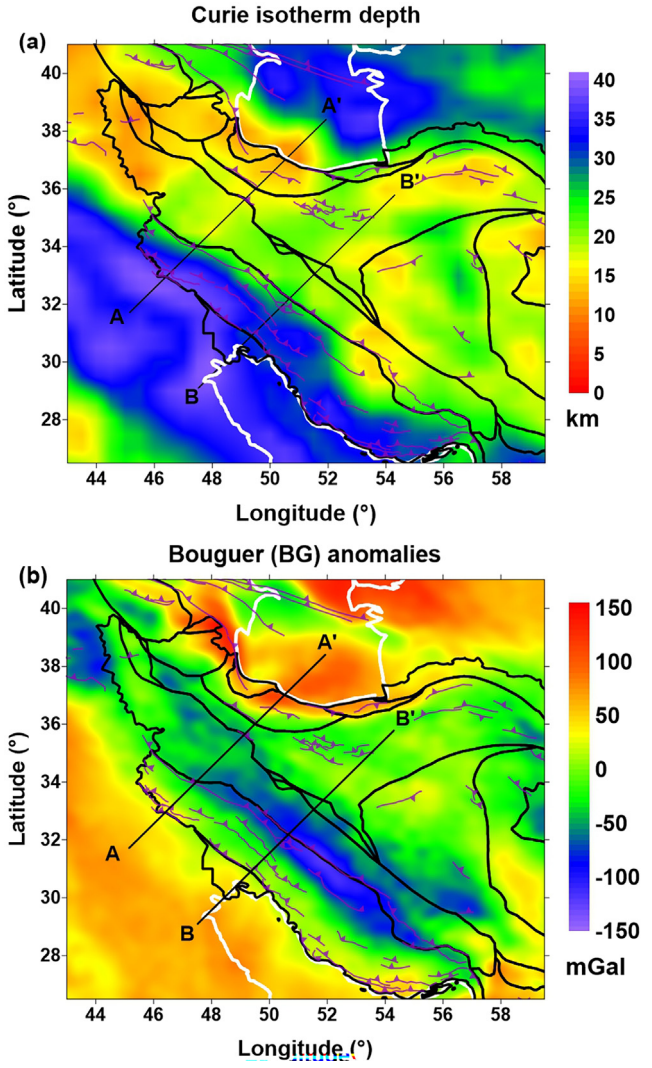

Fig. 3. Magnetic and gravity data for the Zagros region. (a) Depth of the Curie isotherm derived from the inversion of the magnetic anomalies (Li et al., 2017). (b) Bouguer (BG) anomalies obtained from the global gravity model XGM2019e (Zingerle et al., 2020). Thrust faults and tectonic blocks limits are from Rabiee et al. (2019). Black lines show the location of the corresponding cross-sections in Figs. 2, 4 and 5.

Table 1
Correlation coefficients along profiles A-A' and B-B' (see Fig. 4) between surface topography, Moho depth, and Bouguer anomalies. Surface topography and Moho depth are both assumed to be positive values. Sources: (1) surface topography from Amante and Eakins (2009); (2) Moho depth from Kaviani et al. (2020) and Irandoust et al. (2022); and (3) Bouguer anomalies from Zingerle et al. (2020)

Moho depth model and profile	**Correlation coefficients**		
	Topography and Moho depth	*Topography and Bouguer anomaly*	*Moho depth and Bouguer anomaly*
Kaviani et al. (2020) Profile A-A'	0.86	−0.77	−0.92
Irandoust et al. (2022) Profile A-A'	0.76	−0.77	−0.93
Kaviani et al. (2020) Profile B-B'	0.89	−0.86	−0.84
Irandoust et al. (2022) Profile B-B'	0.67	−0.86	−0.83

3.2. Seismicity

The seismic events that occurred between 1906 and 2021 in the studied area (Fig. 1) are characterized by a highly uneven distribution, with most earthquakes concentrated near the ZFBT, with a clear decrease towards the NE, approximately beyond the surface expression of the suture zone (the MZT). In Northern Iran, seismicity is widespread in the Kopeh Dagh, Binalud, and Alborz mountain ranges, indicating that these areas are actively deforming, while in Central Iran it is mainly focused along the boundaries of tectonic micro-blocks, which are instead nearly aseismic (Gao et al., 2022; Rashidi et al., 2022, 2023). The depth of earthquakes ranges from 0 to 183 km, with a body-wave magnitude (Mb) between 4.5 and 7.4. Most of the seismic events have a Mb < 5.0 and occur at a depth < 40 km, while only 10 % of them are located in the deep crust or in the uppermost mantle. The absence of very deep seismicity (>200 km) in the northwestern and central sectors of the Zagros orogen rules out both the presence of a subducting oceanic plate and active continental subduction, consistent with

the *syn*-collisional break-off of the Neo-Tethys slab in the Cenozoic (see Section 2).

Along the collision zone, the frequency of earthquakes increases from NW to SE, as the comparison of the seismicity distributions along the cross-sections A-A' and B-B' clearly shows (Fig. 2). These cross-sections also demonstrate that most of the crustal seismic events are located in the upper (<20 km) and lower (>30 km) parts of the crust. The decrease in seismicity at intermediate crustal depths (~20–30 km) is probably related to ductile rheological conditions that characterize this level. The abrupt lateral reduction in the number of seismic events from SW to NE along cross-section B-B' coincides with the MTZ, where the surface topography begins to decrease and its trend becomes smoother, while the crustal thickness increases, reaching its maximum value (up to ~ 60 km) further to the NE. Along cross-section A-A', such a lateral change in seismic intensity occurs slightly to the NE of the suture zone. The almost complete absence of seismic activity in the SSZ is likely related to the increased thermal conditions (see above), which lead to a predominantly ductile behavior of the thickened continental crust (Koptev et al., 2021) and thus prevent generation of seismic events (Lavecchia et al., 2022). The less abrupt decrease in seismicity in the northwestern sector could be attributed to a more evenly distributed crustal thickening in this part of the orogen (see Section 3.1) and to the proximity to the adjacent tectonically active Alborz mountains. We can also note that the relatively low concentration of seismic events in Central Iran is mostly located at shallower depths than in the ZFTB, likely reflecting a higher rigidity of the upper crust compared to the lower crust and upper mantle in this region (e.g., Gao et al., 2022).

3.3. Depth of the Curie isotherm

The exact thermal structure of the crust and lithospheric mantle is still poorly known in the Iranian region, as most of the area is not covered by surface heat flow measurements, so the only constraints are based on indirect information. In particular, Li et al. (2017) recently inferred the depth of the Curie isotherm (~550 °C) on a global scale from the inversion of the magnetic anomalies of two arc-minute resolution based on fractal magnetization (Fig. 3a). Along the northeastern Arabian margin, the depth of the Curie isotherm ranges from ~ 30 km to ~ 40 km and decreases rapidly toward the NE to ~ 20–15 km depth. In the central and southern part of the collision zone, the abrupt decrease in the Curie temperature depth runs along the boundary delineating the area of high seismicity and mostly coincides with the suture zone (the MTZ), while in the northwestern segment it is slightly shifted to the SW. To summarize, in the Zagros orogen, the shallowing Curie isotherm coincides with a rapid increase in Moho depth (Fig. 2) and is, therefore, probably related to the warming caused by crustal thickening, due to continental collision. In contrast, the shallow depth of the Curie isotherm (~10–20 km) in the Iranian micro-blocks (CEIM), characterized by a much thinner crust compared to the tectonic units forming the collision zone, are possibly the result of bottom-up heating of the overriding plate caused by the upwelling of asthenospheric material through the slab window opened during the detachment of the subducting lithosphere (Gao et al., 2022; Yang et al., 2023b).

3.4. Gravity anomalies

The Bouguer (BG) anomalies, displayed in Fig. 3b, were obtained using the gravity data from the global model XGM2019e (Zingerle et al., 2020), derived from the combination of the satellite-only model GOCO06s (Kvas et al., 2021), satellite altimetry (over oceans), and ground measurements. The model, which is provided in terms of spherical harmonics coefficients, is computed up to degree and order 5399, corresponding to a nominal spatial resolution at the equator of 2′ (approximately 4 km). The source of ground measurements over land is gridded data from the US National Geospatial-Intelligence Agency, which is band-limited to spherical harmonics degree and order 719. The gravity data in the model is augmented using the synthesized signal of topography, which means that the actual maximum resolution of gravity data over land is ~ 30 km at the equator.

Starting from the coefficients in XGM2019e, we computed a gravity disturbance reduced for the gravity effect of topography (Hackney and Featherstone, 2003; Vajda et al., 2008), using the global topography effect model RET2014 (Rexer et al., 2016). The computation of this gravity functional differs from the one used to compute the classical Bouguer anomaly and is aimed at avoiding the "secondary indirect topographic effect", for which we refer to Meurers (2017). However, we refer to it as "Bouguer anomaly" throughout this paper, conforming to the customary nomenclature in geophysics.

The obtained Bouguer (BG) anomalies are in the range of ± 130 mGal. The northeastern part of the Arabian plate is characterized by positive anomalies that decrease in the collision zone (Fig. 3b), in correspondence with the increase in the crustal thickness (Fig. 2). However, the strongest negative anomaly (<-50 mGal), located in the central sector of the collision zone, coincides with the highest topography and is, therefore, shifted to the SW with respect to the maximum crustal thickening. To the NE of the collision zone, both Central and Northeastern Iran are mostly characterized by weak BG anomalies (±50 mGal), due to low topography compensated by a thinner crust. An exception is a strong positive anomaly (>100 mGal) in the Alborz mountains, a peculiar region with a high topography, a relatively deep Moho, volcanic bodies in the crust, and a thin mantle lithosphere.

The observed BG anomalies along transect A-A′ (Fig. 4a) show a relatively high negative correlation (Table 1) with the surface topography trend (−0.77) and even stronger with that of the Moho depth (above −0.90), as expected (Pivetta and Braitenberg, 2020). Along transect B-B′ (Fig. 4b), BG anomalies are also well correlated with surface topography (−0.86) and Moho depth (above −0.80), although the maximum crustal thickness is shifted to the NE with respect to the highest topography and minimum BG anomaly. This shift has been interpreted as a consequence of the lower density of the crust composing the external part of the orogen (the ZFTB), compared to its central and internal part (the SSZ and UDMA), which consists mainly of igneous and metamorphic rocks (e.g., Paul et al., 2006; Maurizio et al., 2023).

3.5. Upper mantle seismic velocities

To examine the structures of the lithospheric and sublithospheric mantle of the Zagros Collision Zone and its surroundings (Fig. 5), we use the surface wave velocity anomalies of the global model SL2013sv (Schaeffer and Lebedev, 2013), which is based on the partitioned waveform inversion technique (Nolet, 1990), and two regional tomography models (Koulakov, 2011; Veisi et al., 2021), which are based on the inversion of travel-time residuals of body waves from earthquakes in the study area. Despite the different resolution of the models and algorithms used to derive the seismic velocities, all three datasets consistently show a sharp lateral transition at a depth of 100 km between the strong positive velocity anomalies, corresponding to the northeastern edge of the Arabian plate and the external part of the collision zone (the ZFTB), and the negative velocity anomalies located further to the NE. The negative anomalies in the upper mantle that characterize most of the Iranian plate are consistent with a thin (<100 km) weakened mantle lithosphere, which underlies the inner part of the collision zone (the UDMA), the adjacent Alborz mountains, and

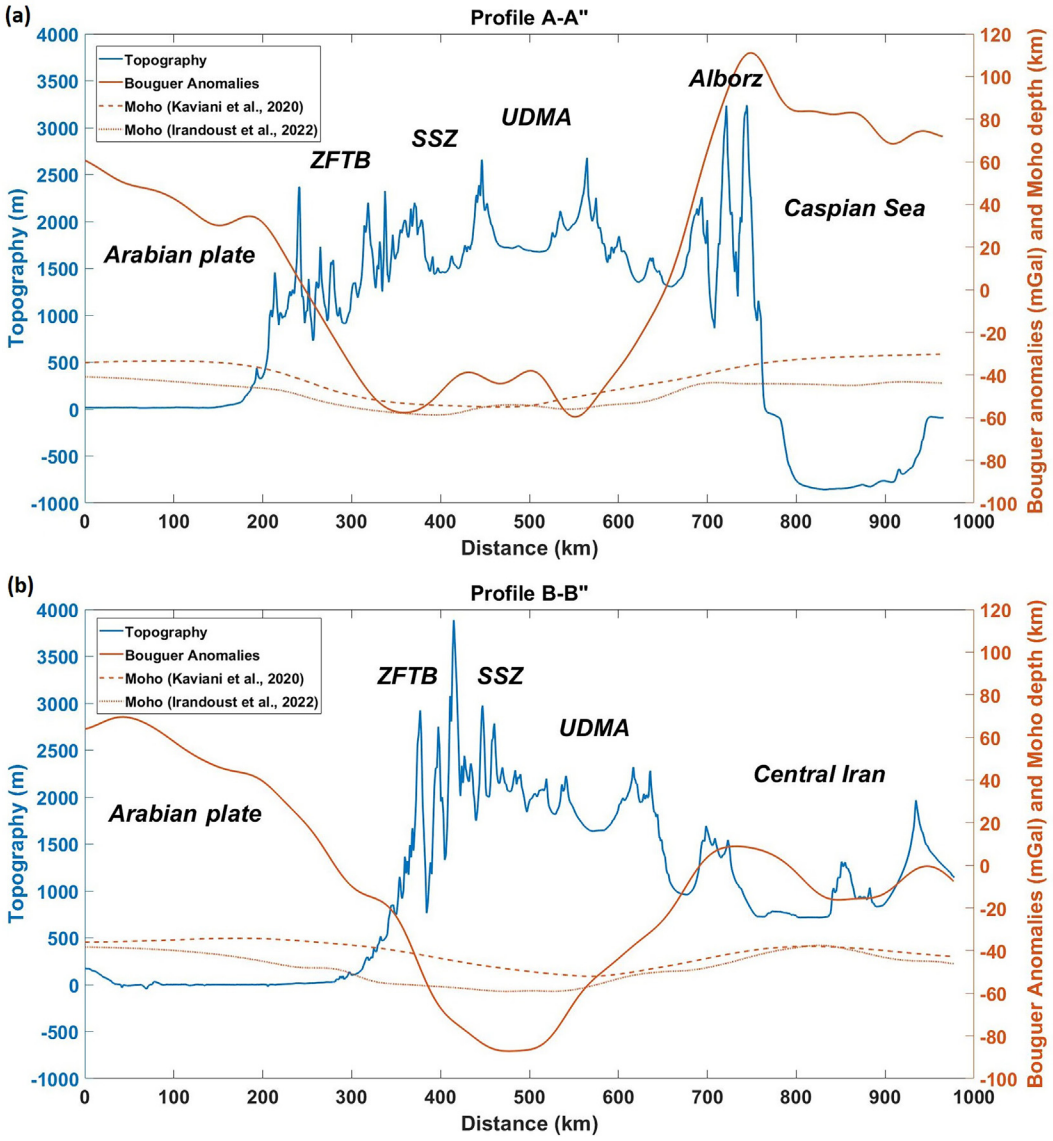

Fig. 4. Variations in surface topography (Amante and Eakins, 2009), Bouguer anomalies (Zingerle et al., 2020), and Moho depth (km) according to the models of Kaviani et al. (2020) and Irandoust et al. (2022), along (a) the northwestern cross-section A-A' and (b) the central cross-section B-B'. The abbreviations correspond to those in Fig. 2.

the micro-blocks composing the Central Iran (e.g., Mahmoodabadi et al., 2019; Motaghi et al., 2015; Mohammadi et al., 2013). This weakening would be the cumulative result of the tectonic processes that occurred during and after the subduction of the Neo-Tethys ocean (see Section 2), such as (1) various phases of slab roll-back leading to extension of the overriding plate; (2) hydration of the mantle wedge due to dehydration of the subducted plate; and (3) upwelling of hot asthenosphere enhanced by the formation of slab windows as a consequence of continental collision (e.g., Mahmoodabadi et al., 2019, 2020; Mohammadi et al., 2013). In the high-altitude areas of the Kopeh Dagh and Binalud mountains, the sign of the anomaly changes from negative to positive, indicating a relative thickening of the lithosphere between the relatively weak Northeastern Iran and the strong Turan Platform (e.g., Motaghi et al., 2017; Wu et al., 2021).

The exact location of the transition between upper mantle positive and negative velocity anomalies, which marks the boundary between the thick (>100 km) underthrusting Arabian lithosphere and thin (<100 km) overriding Iranian lithosphere, changes laterally in the different tomographic studies. In particular, according to the model SL2013sv (Schaeffer and Lebedev, 2013), the edge of the positive anomalies at 100 km depth is oriented in the WNW-ESE direction, oblique to the NW-SE strike of the orogen (Fig. 5a). As a result, the upper mantle underlying the SSZ is characterized by negative and positive anomalies in its northwestern and southeastern parts, respectively. Therefore, in the northern sector of the Zagros, the transition from positive to negative surface wave velocity anomalies is shifted to the SW with respect to the suture zone (the MZT) and roughly follows the abrupt change in Curie temperature depths (see Section 3.1). In contrast, in the southern part of the Zagros, the transition is located NE of the suture, with the positive anomalies covering the entire collision zone (Fig. 5a). Differently from the global model SL2013sv (Schaeffer and Lebedev, 2013), the regional studies (Fig. 5b-c) by Koulakov (2011) and Veisi et al. (2021) show that the boundary between the positive and negative velocity anomalies is aligned parallel to the orogen (NW-SE). Moreover, compared to the model SL2013sv (Schaeffer and Lebedev, 2013), this boundary appears to be shifted to the NE in both the northern and central parts of the Zagros (above 30° latitude). In the southern part, however, the pos-

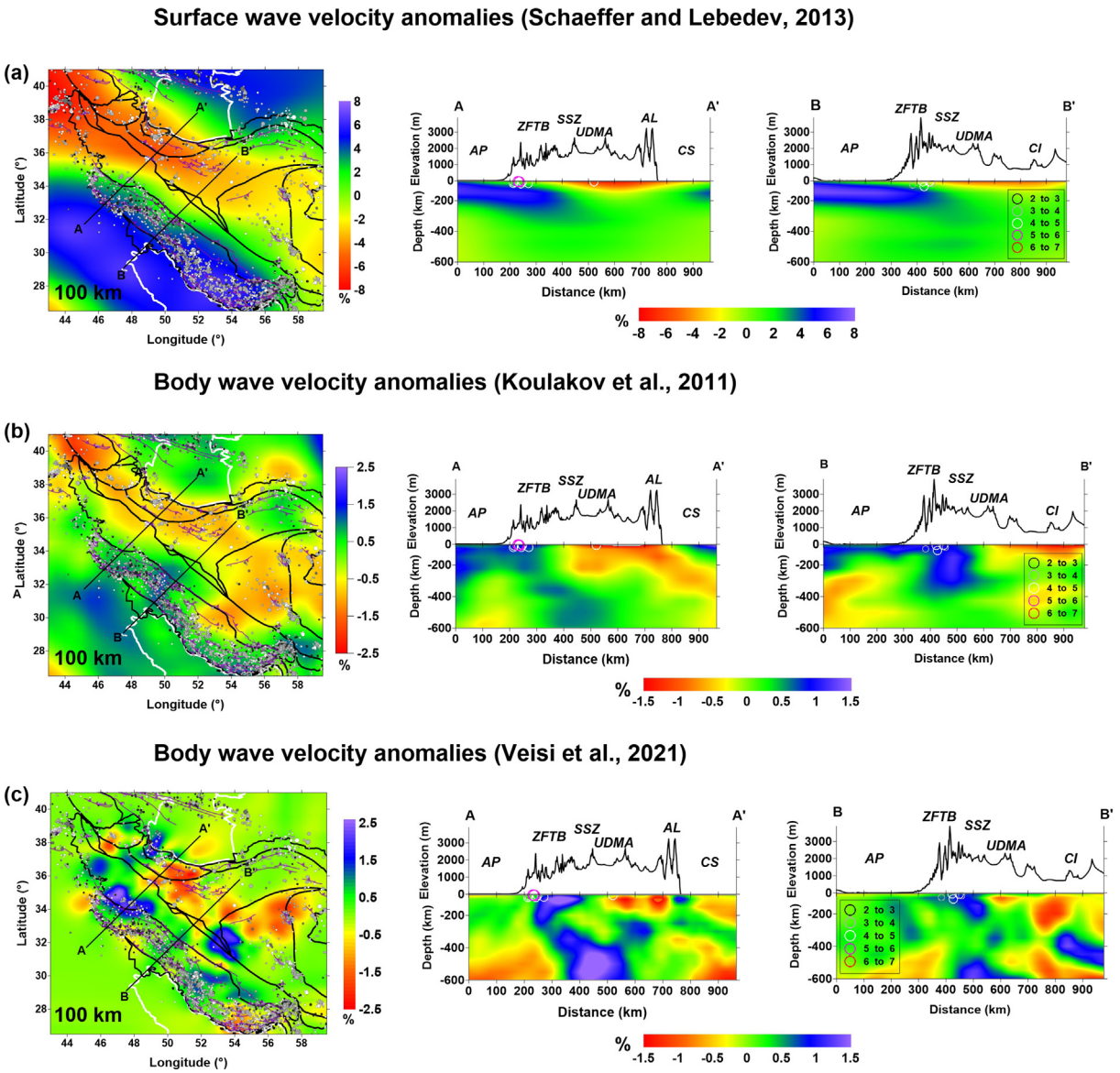

Fig. 5. Seismic wave velocity anomalies from global and regional seismic tomography studies, illustrating the structures of the lithospheric and sublithospheric mantle in the Zagros region. (a) Global surface wave model SL2013sv by Schaeffer and Lebedev (2013). (b) Regional body wave (P-wave) model by Koulakov (2011). (c) Regional shear wave (P-wave) model by Veisi et al. (2021). Velocity anomalies are shown on the horizontal slice at a depth of 100 km and along two cross-sections sections (A-A' and B-B'). Thrust faults and tectonic blocks limits on the maps are from Rabiee et al. (2019). For the representation of earthquakes and abbreviations, the same conventions as in Fig. 2.

itive anomaly in the model of Koulakov (2011) extends laterally only to the inner boundary of the ZFTB and follows the location of the suture zone (Fig. 5b), whereas in the model of Veisi et al. (2021), there is a small negative anomaly beneath the outer part of the SSZ, separating two strong positive anomalies, that indicate the presence of thick lithosphere beneath the ZFTB and the UDMA (Fig. 5c).

The distribution of seismic velocities along cross-section A-A' (northwestern segment of the orogen) shows a continuous strong positive anomaly (presumably corresponding to the subducting slab) down to a depth of at least ~ 250 km in all three models (Fig. 5). In the models of Koulakov (2011) and Veisi et al. (2021), the slab extends horizontally from the Arabian platform and then inclines steeply downward beneath the ZFTB (Fig. 5b) or the external part of the SSZ (Fig. 5c), respectively. The amplitude of the positive anomaly decreases in both datasets at a depth of ~ 250 km and increases ~ 50 km deeper, at ~ 300 km, suggesting the existence of a small gap that divides the slab into two parts (Fig. 5b-c). At greater depths, below ~ 450 km, the positive anomaly increases in amplitude and spatial extent in both models, likely due to buckling and stagnation of the slab in the mantle transition zone (Pons et al., 2022). On the contrary, in the model SL2013sv (Schaeffer and Lebedev, 2013), the Arabian slab gradually tilts down with a small dip angle, while the corresponding positive anomaly clearly loses amplitude at a depth of ~ 250 km and disappears below ~ 400 km (Fig. 5a).

Along cross-section B-B' (central segment of the collision zone), in the global model SL2013sv (Schaeffer and Lebedev, 2013), the slab dips at a lower angle than in cross-section A-A' with a similar reduction in the positive velocity anomaly between ~ 250 km and ~ 400 km (Fig. 5a). Consistently, the regional models (Koulakov, 2011; Veisi et al., 2021) demonstrate a quasi-horizontal penetration of the Arabian plate into the collision zone that is more advanced than in the northwestern section, as the slab only begins to sink to the NE of the MZT directly beneath the SSZ (Fig. 5b-c), which in this segment of the orogen (central Zagros)

is characterized by a relatively smooth topography and the greatest thickness of the crust (see Section 3.1). In the model of Koulakov (2011), the near-vertical subducting slab is continuous to a depth of ~ 400 km, while there are no further positive anomalies in the deeper part of the upper mantle (Fig. 5b). In contrast, the positive anomaly in the model of Veisi et al. (2021) weakens between ~ 250 km and ~ 400 km and becomes strong again below ~ 450 km (Fig. 5c).

Although the results of the three seismic tomography studies are not in complete agreement, they consistently show a shallower dip angle or a more pronounced penetration of the Arabian plate into the collision zone in the central part of the Zagros orogen compared to its northwestern section. In contrast to the interpretations of other seismic tomography and receiver function data, which suggest that the slab break-off occurred in the NW sector of the Zagros (Simmons et al., 2011; Kaviani et al., 2018; Mahmoodabadi et al., 2019; Rahmani et al., 2019; Chang et al., 2010; Vergés et al., 2011), but the slab is still connected to the lithosphere of the Arabian platform in the central and southeastern part of the orogen (Chang et al., 2010; Simmons et al., 2011; Motaghi et al., 2015), the datasets presented here indicate a complete rupture of the subducting plate along the entire Zagros orogen, although the depth and vertical extent of the slab window (s) vary in the different cross-sections and tomography models (Fig. 5). This is generally consistent with the findings of recent numerical experiments showing extremely rapid (tens of cm yr^{-1}) lateral propagation of the initial slab break-off (so-called slab tearing) in the context of both continental collision (Boonma et al., 2023) and continuous oceanic subduction (Andrić-Tomašević et al., 2023).

4. Thermo-mechanical modelling

4.1. Numerical methods and model setup

To investigate the transition from ocean-continent subduction to continental collision phase and the associated process of crustal relamination, we use the 2D thermo-mechanical code I2VIS, which solves the momentum, continuity, and energy equations with a finite-difference scheme on a fully staggered Eulerian grid (Gerya and Yuen, 2003; Gerya, 2019). The physical properties of the different rock types are transported according to the velocity field using the marker-in-cell method. The adopted equations assume compressible material with negligible inertia. The heat equation includes radiogenic, adiabatic, and shear heat sources, as well as latent heat of melting. The processes of (de)hydration, water percolation, melting, melt extraction and melt emplacement are also considered (e.g., Gerya et al., 2002; Vogt et al., 2013).

The deformation is determined by visco-plastic rheology. The viscous (ductile) behavior is described as a combination of dislocation, diffusion, and Peierls creep (the latter two only in the mantle). Plastic/brittle failure is based on the Drucker-Prager yield criterion, also including the effect of strain-induced softening, when the brittle strength decreases linearly with increasing accumulated plastic strain (e.g., Huismans and Beaumont, 2002). The resulting visco-plastic rheologies are assigned on the basis of a Christmas tree-like criterion, in which the effective viscosity is defined as the minimum between the brittle/plastic and ductile components (Burov, 2011). It is important to note that the effective viscosity of rocks is lowered in the presence of water and melt. Hydrated rocks are characterized by a weaker ductile rheology than dry rocks (e.g., wet olivine flow law instead of dry olivine flow law), while partially-molten rocks have an internal friction angle of zero. In addition, the brittle strength is also reduced in the presence of percolating water or melts, due to decreasing effective pressure in rocks below the hydration front (Gerya et al., 2006) or in melt extraction pathways approximated by vertical columns above the melt source (Gerya et al., 2015). The implementation of (de)hydration and melting processes and their effects on the rheological properties of rocks have been described in detail in previous studies (e.g., Gerya and Meilick, 2010; Sheng et al., 2016).

The initial model configuration (Fig. 6) follows the corresponding setup of Maierová et al. (2018), who simulated different subduction-exhumation histories of continental crust, as well as other previous studies exploring the formation of (U)HP rocks (Faccenda et al., 2008; Vogt et al., 2012; Sizova et al., 2012; Dymkova et al., 2016). The model domain is 4000-km wide and 1000-km deep. The spatial resolution of the experiments is 1×1 km around the contact between the subducting and overriding plates, while it decreases gently further away from this part of the model. The subducting plate is composed of continental and oceanic parts. In most experiments, the continental crust of the subducting plate consists of evenly divided felsic (upper) and mafic (lower) layers with a total thickness of 30 km. We have additionally tested an upper crust thickened by 10 km and rheological properties corresponding to felsic composition for the entire crust including the lower layer (see below). The oceanic crust contains basaltic (2 km thick) and gabbroic (5 km thick) layers. The continental crust of the overriding plate is also composed of an upper felsic layer and a lower mafic layer (20 km and 10 km thick, respectively). The initial lithospheric and sublithospheric mantle is assumed to be of dry olivine composition. To facilitate the onset of subduction (Stern and Gerya, 2018), we prescribe a sedimentary wedge and a weak zone of hydrated mantle at the contact between the subducting and overriding plates (e.g., Koptev et al., 2022). The ductile flow laws and reference densities for all rock types are summarized in Table 2, while we refer to Maierová et al. (2018) for further details on the values of individual parameters.

All boundaries of the experimental domain are modelled as free-slip rigid walls. The deformed stress-free surface of the Earth is approximated using the "sticky-air" method (Schmeling et al., 2008; Crameri et al., 2012). Elevation-dependent erosion and sedimentation act at the interface between the "sticky-air" and the "rock" (Gorczyk et al., 2007). The convergence of the subducting and overriding plates is determined by a constant velocity associated to the subducting plate throughout the model evolution (Fig. 6). Temperatures at the top and bottom of the model are constant (0 °C and 1790 °C, respectively), while thermally insulating boundary conditions (a conductive heat flux of zero) are imposed on the left and right boundaries. For the oceanic lithosphere, the initial temperature distribution is defined by the half-space cooling approximation (Turcotte and Schubert, 2002). In the continental domain, we apply a typical steady-state conductive geotherm (Artemieva, 2006; Koptev and Ershov, 2011). The adiabatic gradient in the sublithospheric mantle is 0.5 K/km (Sleep, 2003; Putirka et al., 2007).

Overall, we performed 19 experiments by varying 8 control parameters (Table 3), which include (1) initial thermal age of the oceanic plate (20–100 Myr); (2) initial width of the oceanic lithosphere (500–900 km); (3) convergence rate (3–5 cm yr^{-1}), (4–5) thermal thickness of the continental lithosphere in the overriding (55–65 km) and subducting (110–150 km) plates; (6–7) thickness (30–40 km) and strength (mafic or felsic rheology for lower layer) of the subducting-plate continental crust; and (8) presence or absence of a thinned continental segment at the original passive margin. The range of values for the tested parameters was chosen in accordance with those reported in the literature (e.g., Boutoux et al., 2021; Darin and Umhoefer, 2022), taking into account unavoidable uncertainties in quantitative evaluations based on different reconstructions. Furthermore, we also considered heterogeneities along strike of the Zagros orogen (i.e. in the direction

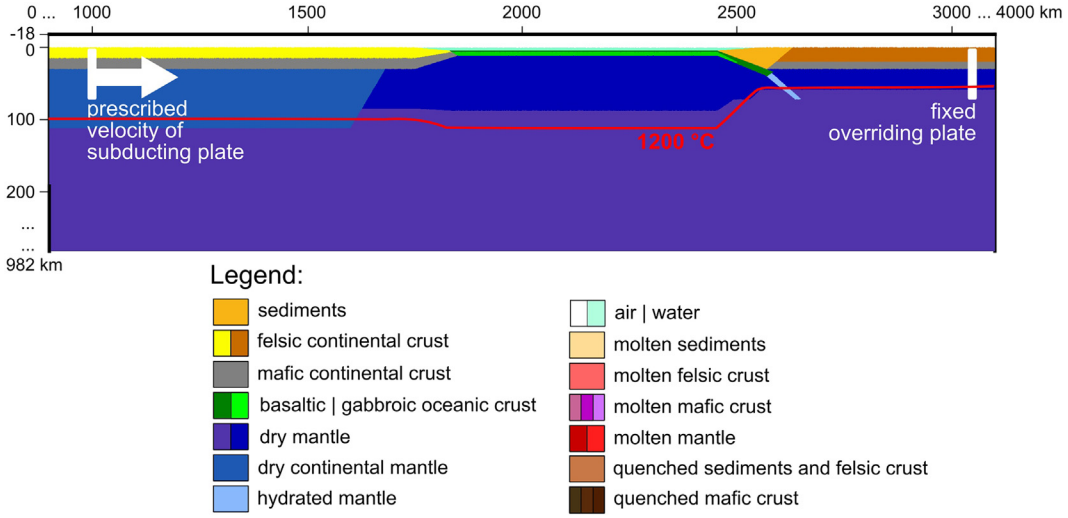

Fig. 6. Initial model setup. The model area consists of an overriding continental lithosphere and a subducting lithospheric plate, containing both oceanic and continental lithosphere. The entire model domain is 4000 × 1000 km, with only the uppermost 300 km shown (note also the vertical scale exaggeration). The color coding defined in the legend is used throughout the paper. Hydrated, partially molten and quenched rocks appear over the evolution of the experiments (see Figs. 7-12; Figs. S4-S6). The red line shows the initial isotherm of 1200 °C for the reference model M1. (For interpretation of the references to color in this figure legend, the reader is referred to the web version of this article.)

Table 2
Densities and ductile flow laws used in thermo-mechanical modelling for individual rock types. Sources for rheological parameters: (1) crustal rocks from Ranalli (1995); and (2) mantle rocks from Karato and Wu (1993), Evans and Goetze (1979), and Katayama and Karato (2008). Note the relatively low density of the felsic continental crust, which favors its exhumation and is thus relevant to the relamination process (see Maierová et al., 2018). This is also consistent with the observation of a less dense crust in the external part of the Zagros orogen, composed by deformed sediments that were deposited on the Arabian continental margin before the continental collision (see Section 3.1).

Rock type	Reference density (kg/m3)	Viscosity (flow law)
sediments	2900	wet quartz
felsic crust	2700	wet quartz
mafic crust	3000	anorthite
basaltic oceanic crust	3000	wet quartz
gabbroic oceanic crust	3000	anorthite
molten sediments, felsic crust	2500	wet quartz
molten mafic crust	2500	anorthite
molten basalt	2500	wet quartz
molten gabbro	2900	anorthite
dry mantle	3300	dry olivine
dry continental mantle	3200	dry olivine
hydrated mantle	3300	wet olivine
molten mantle	2900	dry olivine

perpendicular to the plane of our 2D models) caused by variations in the properties of colliding plates and the obliquity of continental collision during the gradual closure of the Neo-Tethys ocean from NW to SE (see Section 2).

For each model, the horizontal variations in the surface topography and Moho depth were defined on the basis of density (*iso*-density 2000 kg/m^3) and material distribution (top of lithospheric mantle), respectively (Figs. S1-S2). Since the Moho depth in the vicinity of the trench can be unrealistically deep due to the complexity of the structures formed there, a maximum possible Moho depth is arbitrarily limited by a value of 80 km. We also estimated the width of the collision-generated orogens (surface elevation of > 1 km) and the lateral extent of their deepest crustal roots (Moho depth of 80 km) and then linked these parameters to the maximum heights of the topography (Fig. S3; Table 4).

We compare the modelling results with the observations at the "final" time of each simulation, when the continental margin of the subducting plate reaches a depth of 200 km, a value consistent with geologic constraints (e.g., Darin and Umhoefer, 2022). The duration of experimental period, therefore, varies from one model to another (Table 3).

4.2. Results of the numerical models

4.2.1. Reference model M1

The model M1, taken as a reference, is characterized by an initial age and width of the oceanic subducting plate of 80 Myr and 700 km, a convergence rate of 4 cm yr^{-1}, which is consistent with previous estimates (e.g., Boutoux et al., 2021), and a 60 km thick overriding plate, in agreement with the seismic tomography data discussed above, showing a thin lithosphere of the Iranian plate (Koulakov, 2011; Schaeffer and Lebedev, 2013; Veisi et al., 2021).

The model evolution begins with an oceanic subduction that lasts ~ 20 Myr. During this stage, an initial period of trench advance and associated topographic build-up (Fig. 7a) changes to trench retreat and overriding plate extension, leading to boudinage of the mafic lower crust, decrease in topographic height, and basin formation (Fig. 7b). In the subduction zone, sediments and part of the oceanic crust are scraped from the oceanic plate and mixed with the felsic crust of the overriding continental plate. This additional buoyant material accumulates near the trench and contributes to the growth of the topography over this region. With the arrival of the continental margin, the trench advance starts again, resulting in predominant compression in the overriding continent (Fig. 7c). The subsequent continental subduction causes a pronounced uplift of the topography. The subducted felsic crust warms up, becomes weaker, detaches from the rest of the plate, flows laterally and is emplaced (relaminated) below the lower crust of the overriding plate (Fig. 7d). The resulting felsic relaminant crust, which correlates with a prominent topographic rise at the distance of ~ 200 km from the trench, advances towards a gap between the mafic boudins (Fig. 7e) that formed during the extension of the overriding plate in the early phase of system evolution (Fig. 7b). In its final state (~32 Myr after the start of the experiment), the elevated topography of the orogen is ~ 300 km

Table 3
Control parameters and duration of experimental period for the thermo-mechanical models.

Model names	Control parameters								Model duration (Myr)
	Subducting oceanic lithosphere		Convergence rate (cm yr^{-1})	Total thickness of overriding continental lithosphere (km)	Subducting continental lithosphere				
	Initial age (Myr)	Initial width (km)			Total thickness (km)	Crustal thickness (km)	Lower crust rheology (S – strong; W – weak)	Thinned margin (N – no; Y – yes)	
M1	80	700	4	60	110	30	S	N	32
M2	20	700	4	60	110	30	S	N	26
M3	40	700	4	60	110	30	S	N	27
M4	60	700	4	60	110	30	S	N	30
M5	100	700	4	60	110	30	S	N	35
M6	80	500	4	60	110	30	S	N	25
M7	80	900	4	60	110	30	S	N	38
M8	80	700	3	60	110	30	S	N	41
M9	80	700	5	60	110	30	S	N	26
M10	80	700	4	55	110	30	S	N	43
M11	80	700	4	65	110	30	S	N	26
M12	80	700	4	60	150	30	S	N	31
M13	80	700	4	60	110	40	S	N	32
M14	80	700	4	60	110	30	W	N	30
M15	80	700	4	60	110	30	S	Y	32
M16	60	500	4	60	110	30	S	N	24
M17	100	900	4	60	110	30	S	N	43
M18	60	900	4	60	110	30	S	N	37
M19	100	500	4	60	110	30	S	N	29

Table 4
Output parameters of the thermo-mechanical models describing the resulting topography and crustal thickness, as well as the modelled Bouguer (BG) anomalies. The width of the orogen is defined as the distance between the two farthest points having a surface elevation of ≥ 1 km. The width of the deep Moho corresponds to the distance between the two farthest points with a maximum permissible depth of 80 km. The width of the minima BG anomaly is determined as the distance between the two farthest points falling in the lowest 10 % of the distribution (thin black lines in Fig. 13).

Models Name	Width orogen (km)	Maximum elevation (km)	Width deep Moho (km)	Width minima BG anomaly (km)	Minima BG Anomaly (mGal)
M1	312.5	7.3	135.5	165	−417.2
M2	207.5	5.1	28	66	−402.4
M3	230.5	5.9	36	81.5	−434.4
M4	256.5	6.5	150	67.5	−425.2
M5	342	7.2	156	134	−532.1
M6	283.5	5.3	50	90	−442.4
M7	290.5	5.6	127.5	64.5	−584.6
M8	261.5	6.2	104	57.5	−495.6
M9	323	6.7	152	107	−478.5
M10	377	9.1	227	133.5	−604.2
M11	170	7.2	21	70.5	−364.6
M12	304.5	7.7	146	73.5	−460
M13	337	7.3	169	82.5	−443.3
M14	298.5	7.1	10.5	132	−325.2
M15	341.5	6.3	147	96	−545.3
M16	281.5	6.6	56	71.5	−505.3
M17	349	7.3	134	136	−560.6
M18	252.5	8.2	134.5	93	−535
M19	325	5.8	48	178.5	−446.3

wide (Fig. S1; Table 4) and has several peaks related to (1) the sedimentary mélange near the trench; (2) the gap in the mafic crust hosting the felsic relaminant; and (3) a tectonically raised crust at the internal margin of the orogen (Fig. 7e).

The resulting crustal structure and composition is also reflected in the viscosity distribution, which shows an alternation of low and high viscosity corresponding to felsic and mafic bodies (Fig. 7e, right column). The lowermost crust reaches temperatures of ∼ 700 °C and is subject to partial melting (violet color in Fig. 7e, left column). Beneath the orogenic crust, the overriding lithospheric mantle is intensively buckled, locally hydrated and partially molten (light blue and red colors in Fig. 7e, left column).

4.2.2. Effect of oceanic plate age (models M2-M5)

Different initial ages of the subducting oceanic lithosphere imply a difference not only in the initial density and thermal thickness (Turcotte and Schubert, 2002), but also in the rheological properties (Burov, 2011). As shown by the experiments in which we varied the oceanic age between 20 Myr and 100 Myr (models M2-M5; Fig. 8), the age-related plate stiffness appears to have the greatest influence on the subduction angle. Since the mechanical strength of the oceanic lithosphere decreases with decreasing age (in other words, younger slabs are weaker than older ones), the plate with an initial age of 20 Myr (model M2; Fig. 8a) bends more easily and, therefore, subducts more steeply than the older plates in other experiments (models M3-M5; Fig. 8b-d).

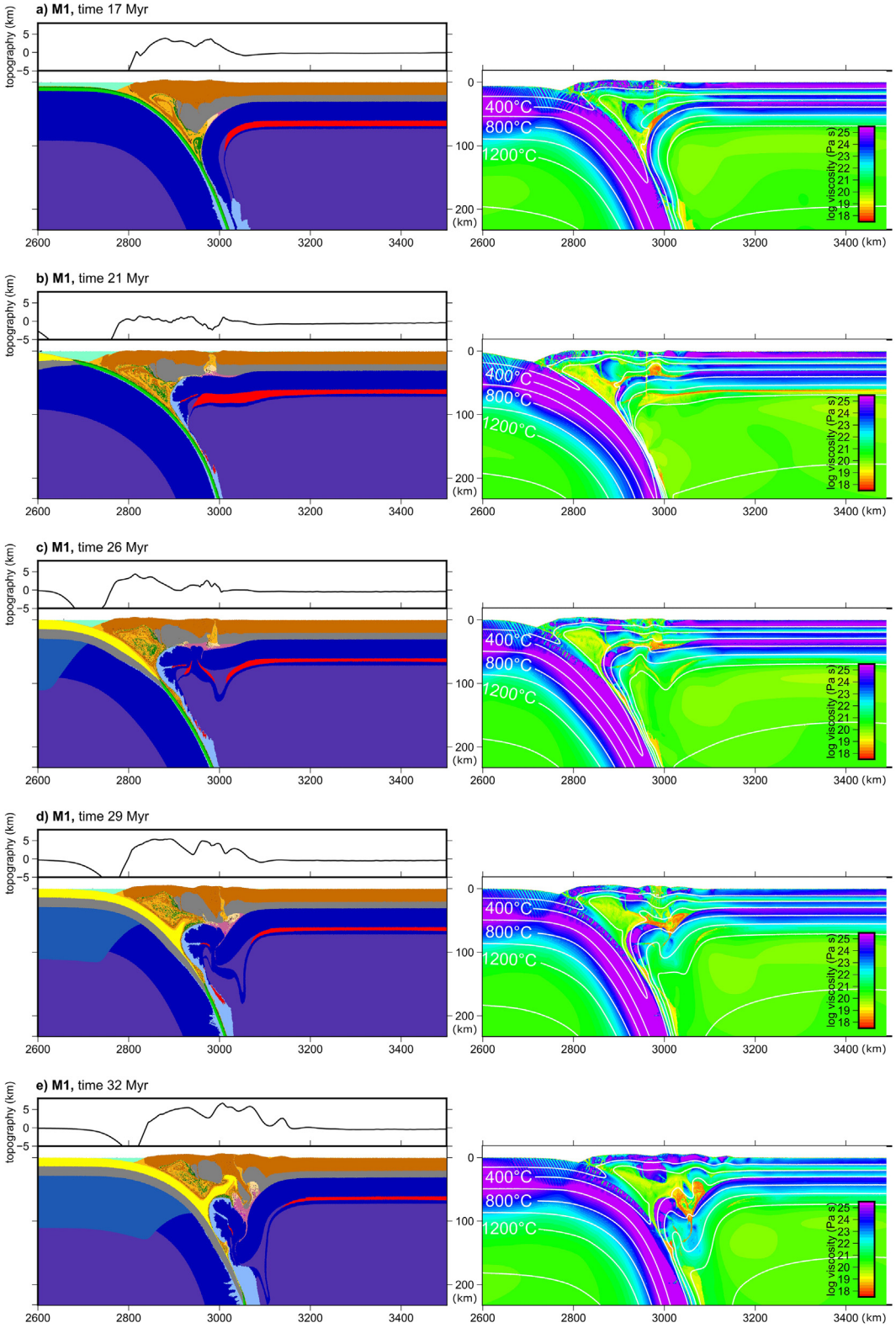

Fig. 7. Temporal evolution of reference model M1 (Table 3) showing the transition from (a-b) ocean-continent subduction to (c) continent–continent subduction and (d-e) collision, accompanied by intra-crustal relamination. Left panels: compositional fields with surface topography (black lines on top); right panels: viscosity distributions overlapped by isotherms from 200 ℃ to 1400 ℃ (white lines). Note that the initial topography variations are already visible in the early stages of subduction, due to the deformation of the positively buoyant sediments that have accumulated in the trench (panels "a" and "b"). However, as soon as the continental part of the lower plate begins to subduct (panel "c") and especially when the felsic crust of the subducting plate is relaminated into the crust of the overriding continent, the uplift of the topography becomes more pronounced (panels "d" and "e").

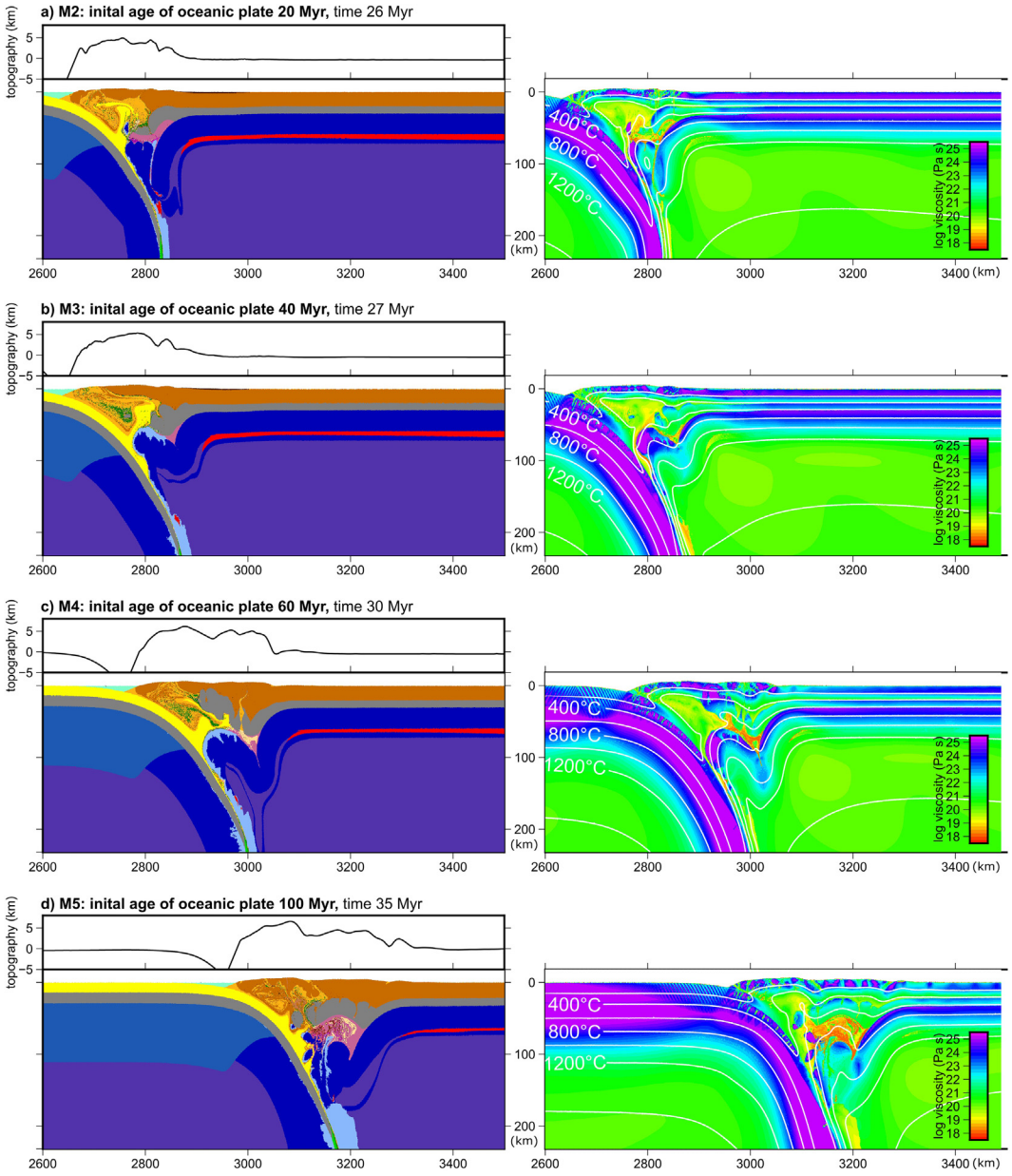

Fig. 8. Models M2-M5, which are characterized by variable initial age of the oceanic subducting plate: (a) 20 Myr, (b) 40 Myr, (c) 60 Myr, and (d) 100 Myr. The compositional fields (left panels) and viscosity distributions (right panels) are shown at the final time (Table 3) of evolution of the corresponding experiments (the same applies to Figs. 9-12 below).

During the phase of ocean-continent subduction, the more steeply dipping slab in the experiments M2 and M3 (oceanic plate age of 20 and 40 Myr, respectively) results in a faster roll-back and, therefore, in a stronger extension of the overriding plate, which is localized in the area near the trench. The subsequent continental collision leads to a relamination of the felsic crust, which overthrusts on the lower crust within the overriding continental lithosphere (Fig. 8a-b). Compared to the reference model (Fig. 7e), this relamination has a limited horizontal extent and is accompanied by the formation of relatively narrow (<250 km wide) and low elevated (<6 km) orogens (Table 4), that are subject to small topographic undulations (<1 km). These short-wavelength topographic variations (Fig. S1a) are due to the combined effect of the low density and viscosity of the accreted sediments and the relaminated felsic crust, which localize brittle deformation (corresponding to high values in the viscosity field) in the uppermost part of the crust (Fig. 8a-b, right column).

A shallower subduction of an older oceanic slab (60 Myr; model M4) produces a different style of relamination, where the felsic crust detached from the downgoing plate intrudes between the mafic crust and lithospheric mantle of the overriding plate (Fig. 8c), similar to the reference model M1 (Fig. 7e). In the case of the oldest subducting plate (80 Myr; model M5), relamination is not well developed, as most of the upper crustal material continues to subduct together with the downgoing slab. However, due to the shallowest subduction angle, the crust of the overriding plate undergoes pronounced shortening and internal deformation, resulting in the widest (~350 km) and highest (>7 km) orogen (Table 4), despite the lack of relaminants (Fig. 8d). The large-scale topographic variations of this orogen (Fig. S1a) may reflect the long-wavelength deformation of the mafic lower crust, which in this case tends to be rheologically coupled with the overlying stiff upper crust, forming a thick high-viscosity layer (Fig. 8d, right column). A similar tendency to link small-scale topographic

undulations with pronounced relamination and longer-scale relief variations with strong but highly deformed crust can also be observed in the other experiments (see below).

4.2.3. Effect of oceanic plate width (models M6-M7)

The increase (decrease) in the width of the oceanic plate implies a longer (shorter) period of ocean-continent subduction and thus a relatively older (younger) oceanic slab at the time of the continental collision. Therefore, experiments M6 and M7 with an ocean width of 500 km and 900 km (Fig. 9) show a contrast in the resulting dip angle, which is smaller in the latter case, due to the longer cooling and strengthening. In agreement with the results of the models discussed above (see Section 4.2.2), shallower subduction leads to the formation of a more uniformly wide orogen, which is similar in characteristics to that of the reference model (compare models M1 and M7 in Table 4). Individual mafic blocks (boudins), underthrust by a felsic relaminant and sedimentary mélange, are pushed upwards to the shallowest levels of the overriding plate (Fig. 9b). The resulting inverted viscosity distribution, with a high-viscosity upper part underlain by deep low-viscosity roots (Fig. 9b, right column), fits well with recent seismic tomography for the central part of the Zagros orogen (Talebi et al., 2020). In contrast, the experiment M6 with a narrow (initially 500-km wide) oceanic basin (Fig. 9a) shows no pronounced relamination and only limited thickening of the crust (see Table 4 and Fig. S2b).

In addition, the increasing width of the oceanic plate causes a longer duration of ocean subduction and cooling of the upper plate. During the subduction of the 900-km wide ocean (model M7; Fig. 9b), the cooling and stiffening of the upper plate contributes to the formation of an orogen with a more uniform surface topography and wider deep roots (>100 km; Fig. 9b; Fig. S1b, S2b, and S3b; Table 4).

4.2.4. Effect of convergence rate (models M8-M9)

The change in the convergence rate (models M8 and M9; Fig. 10a-b) has several competing effects on the shape of the formed orogen and the internal structure of the crust in the collision zone. The rate of closure of the oceanic basin between the two continents influences the duration of the oceanic subduction phase and thus the age of both plates (subducting and overriding) at the onset of continental subduction and collision. The increase in the convergence rate to 5 cm yr^{-1} (model M9; Fig. 10b) has a twofold effect. On the one hand, the oceanic slab is younger at the time of the collision, so that the style of relamination – overthrusting of the felsic relaminant on the lower crust in a horizontally limited area near the trench – is similar to that of the model with an originally young oceanic plate (Fig. 8a). On the other hand, an overriding continental plate, which is also younger and weaker (compare the thickness of the molten zone at the base of the lithosphere at the last time step in the different models), undergoes more intense deformation, that spread over a greater distance from the trench and results in a wider orogen (Fig. S1c).

In the case of a slower convergence rate (3 cm yr^{-1}; model M8), the residence time of the continental crust in contact with the warm mantle during continental subduction is longer and the warmer upper crust detaches more easily from the rest of the subducting plate and exhibits higher mobility, allowing the relaminated felsic material to rise vertically almost to the surface (Fig. 10a). Interestingly, relamination remains close to the trench at both lower (3 cm yr^{-1}; model M7) and higher (5 cm yr^{-1}; model M8) convergence rates (Fig. 10a-b), in contrast to the reference model (model M1) with the intermediate value of 4 cm yr^{-1}, where the relaminant advances much further into the interior of the overriding plate (Fig. 7e).

4.2.5. Effect of overriding plate thickness (models M10-M11)

Relatively small deviations in the thermal thickness of the overriding continental lithosphere of ± 5 km (models M10 and M11) compared to the reference value of 60 km (model M1) have a profound influence on its rheological properties and the resulting style of continental collision and relamination (Fig. 10c-d). In particular, the thinner (and, therefore, weaker) overriding plate (total thickness of 55 km; model M10) is subject to greater extension during oceanic plate subduction and more

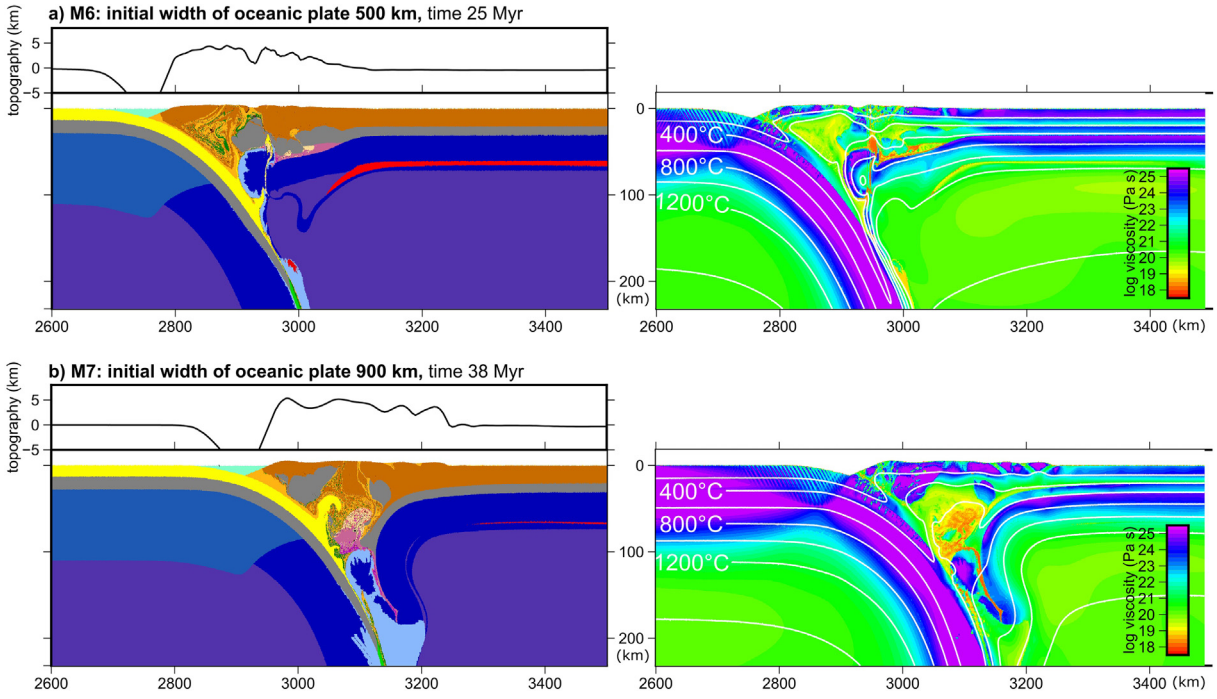

Fig. 9. Models M6-M7, which are characterized by variable initial width of the oceanic subducting plate: (a) 500 km and (b) 900 km.

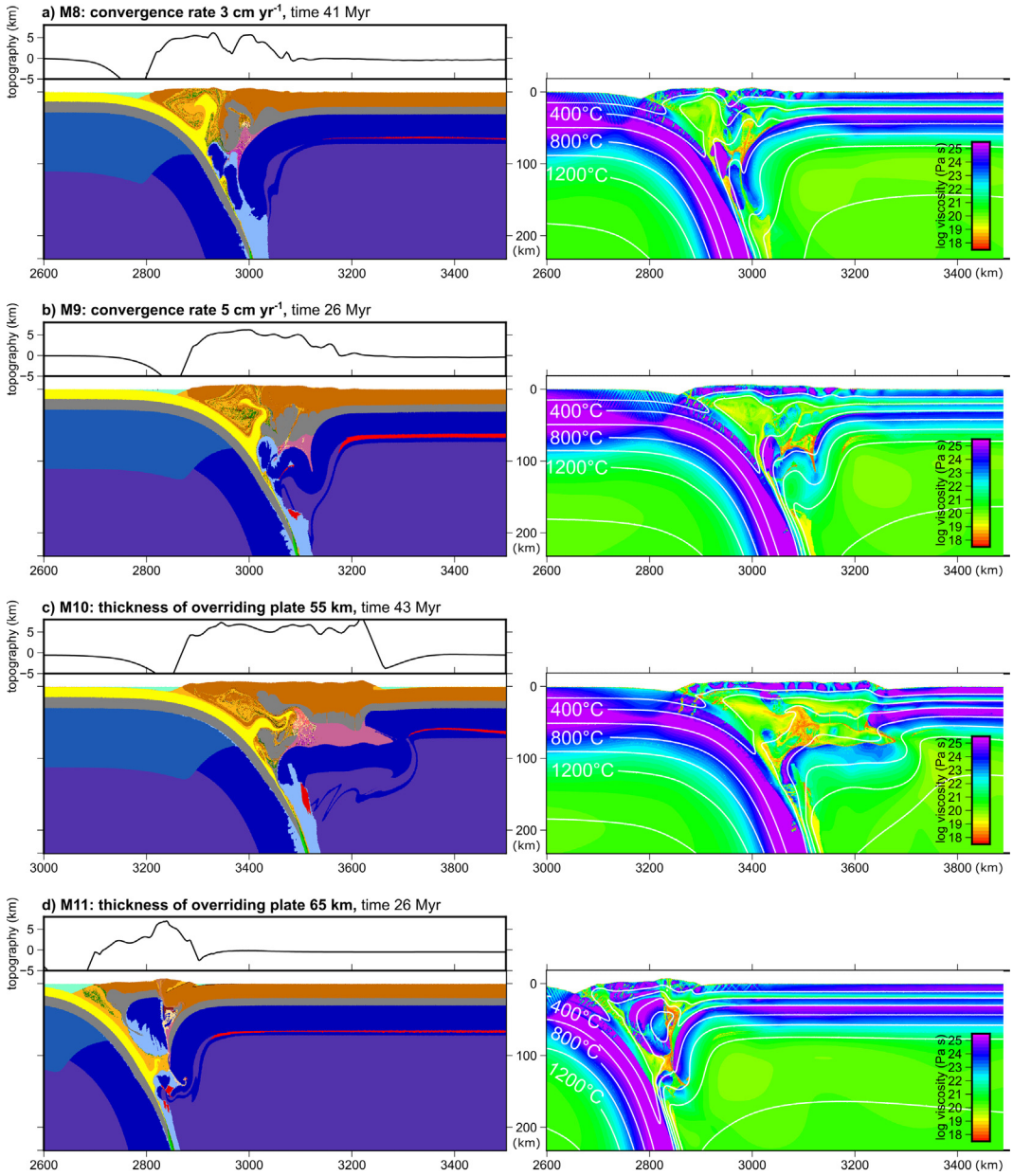

Fig. 10. Models M8-M11, which are characterized by variable convergence rate: (a) 3 cm yr^{-1} and (b) 5 cm yr^{-1}, and thermal thickness of the overriding continental lithosphere: (c) 55 km and (d) 65 km.

pronounced compression during continental collision. The resulting deformation of both the crust and mantle lithosphere, which extends well beyond the near-trench zone, produces the widest (~400 km) and highest (maximum height of >9 km) orogen (Table 4; Fig. S1d), with large (>200 km) and deep crustal roots (Fig. S2d) that are partially molten over a vast area (Fig. 10c). In contrast, the increase in thickness of the upper plate to 65 km (model M11) leads to higher integrated strength with the consequent localization of deformation in a narrow segment close to the trench and extremely limited relamination of the lower-plate felsic material, most of which remains attached to the subducting slab (Fig. 10d). The resulting narrow orogen, which is only 170 km wide (Table 4), is underlain by an extremely thickened crust (the uncut modelled Moho depth is >100 km) that contains a large high-viscosity region (Fig. 10d, right column) composed by locally hydrated lithospheric mantle (Fig. 10d, left column).

4.2.6. Effect of specific parameters for subducting continent (models M12-M15)

The processes of continental collision and crustal relamination depend not only on the thickness of the overriding continent, age and width of the subducting ocean, and rate of convergence between them (Figs. 8–10), but also on the properties of the continental part of the subducting plate (Fig. 11), coming into contact with the continental overriding plate during the collision phase.

In particular, an increase in the thermal thickness of the continental lithosphere on the subducting plate from the reference value of 110 km to 150 km (model M12) produces a stiffer continental margin that bends at a lower dip angle. The resulting topography (Fig. S1e) and general style of relamination (Fig. 11a) remain the same as in the reference model M1 (Fig. 7e), with the only exception that the gap between the mafic boudins of the stretched lower crust, which is filled with uplifted felsic relaminant, is slightly closer to the trench in model M12.

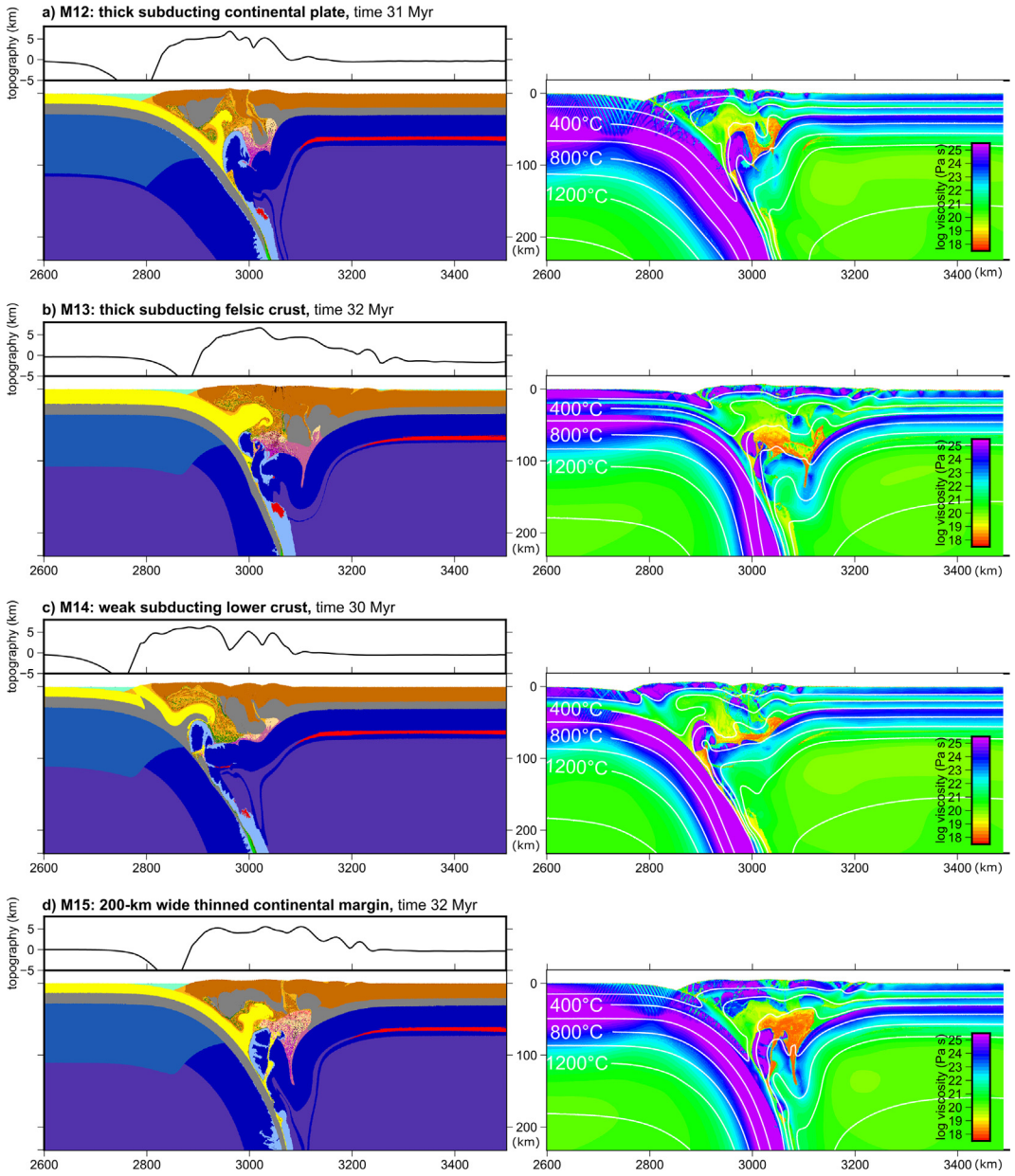

Fig. 11. Models M12-M15, which are characterized by specific parameters for the continental part of the subducting plate: (a) a higher value of lithospheric thermal thickness (150 km), (b) a thicker continental crust (40 km), (c) a weaker (felsic) rheology of the lower crustal layer, and (d) the presence of a thinner 200 km wide segment at the boundary with the oceanic lithosphere (rifted continental margin).

A thickening of the upper crust of the continental lithosphere by 10 km, leading to an increase of the total crustal thickness from 30 to 40 km (model M13), expectedly provides a larger amount of relaminated felsic material, which accumulates mainly in the near-trench area (Fig. 11b), forming above a high (>7 km) surface topography (Fig. S1e). The internal part of the orogen is underlain by a thick crust with highly deformed mafic blocks, the upper part of which corresponds to the high-viscosity anomalies, while the lower segments are partially molten (Fig. 11b, left column) and weak (Fig. 11b, right column). The resulting orogen is broad (Table 4; Fig. S1e) both in terms of crustal roots (>150 km) and topography (>300 km).

In the experiment M14, we apply the wet quartzite flow law to the ductile properties of the entire continental crust, including the lower mafic layer, which is characterized by a stronger anorthite rheology in all other models (Table 2). The weaker crust leads to detachment and relamination of both the felsic and mafic layers, although the lower crust undergoes these processes to a much lesser extent, due to its higher density (Fig. 11c). Similar to the previous model M13, the relaminated material pushes the boudins of the lower crust towards the continental interior, increasing crustal viscosity in the internal part of the orogen (Fig. 11c, right column). In general, the orogenic crust is relatively thin with an extremely narrow (only 10 km) segment of deep (where Moho depth is $\geq$ 80 km) roots (Table 4; Fig. S2f).

The inclusion of a 200 km wide segment of thinned continental lithosphere at the boundary with the oceanic segment of the subducting plate (model M15; Fig. 11d) does not generate significant deviations in the shape of the orogen and the style of relamination, with respect to the reference model M1, without such an extended margin (compare Fig. 7 and S4). The only effect of the thinned passive margin in model M15 is a slight increase in the buoyancy of

the subducting plate and volume of the relaminated felsic crust (Fig. 11d; Fig. S4).

4.2.7. Combined effects of oceanic plate age and width (models M16-M19)

In contrast to the previously described models M2-M15, in which only one parameter was changed from its reference value in experiment M1, we also performed models M16-M19, in which the age and width of the initial oceanic lithosphere were changed simultaneously to investigate the combined impact of these parameters on the modelling results (Fig. 12).

Model M16 (Fig. 12a) with a relatively young (60 Myr) and narrow (500 km) ocean shows no relamination, similarly as the experiment with an originally narrow oceanic basin (model M6; Fig. 9a), and a moderate width (<300 km) of the resulting orogen, which is typical for all other models with oceanic plates younger than the reference (models M2-M4; Fig. 8a-c; Table 4). According to the model M17, an old (100 Myr) and wide (900 km) oceanic domain leads to opposite results with a pronounced relamination of felsic material overthrusting on the mafic lower crust and with the formation of a broad (~350 km) orogen, with two maxima of elevation, corresponding to its most external and internal part (Fig. 12b; Fig. S1g).

In the case of a young (60 Myr) and wide (900 km) oceanic plate (model M18), the relamination proceeds differently: the felsic material of the subducting plate penetrates into the lowermost part of the crust of the upper plate and underlies (together with a sedimentary mélange) the stretched mafic layer (Fig. 12c; Fig. S5). The resulting orogen is slightly narrower (~250 km) than in the reference case (Table 4). In contrast, an oceanic subducting

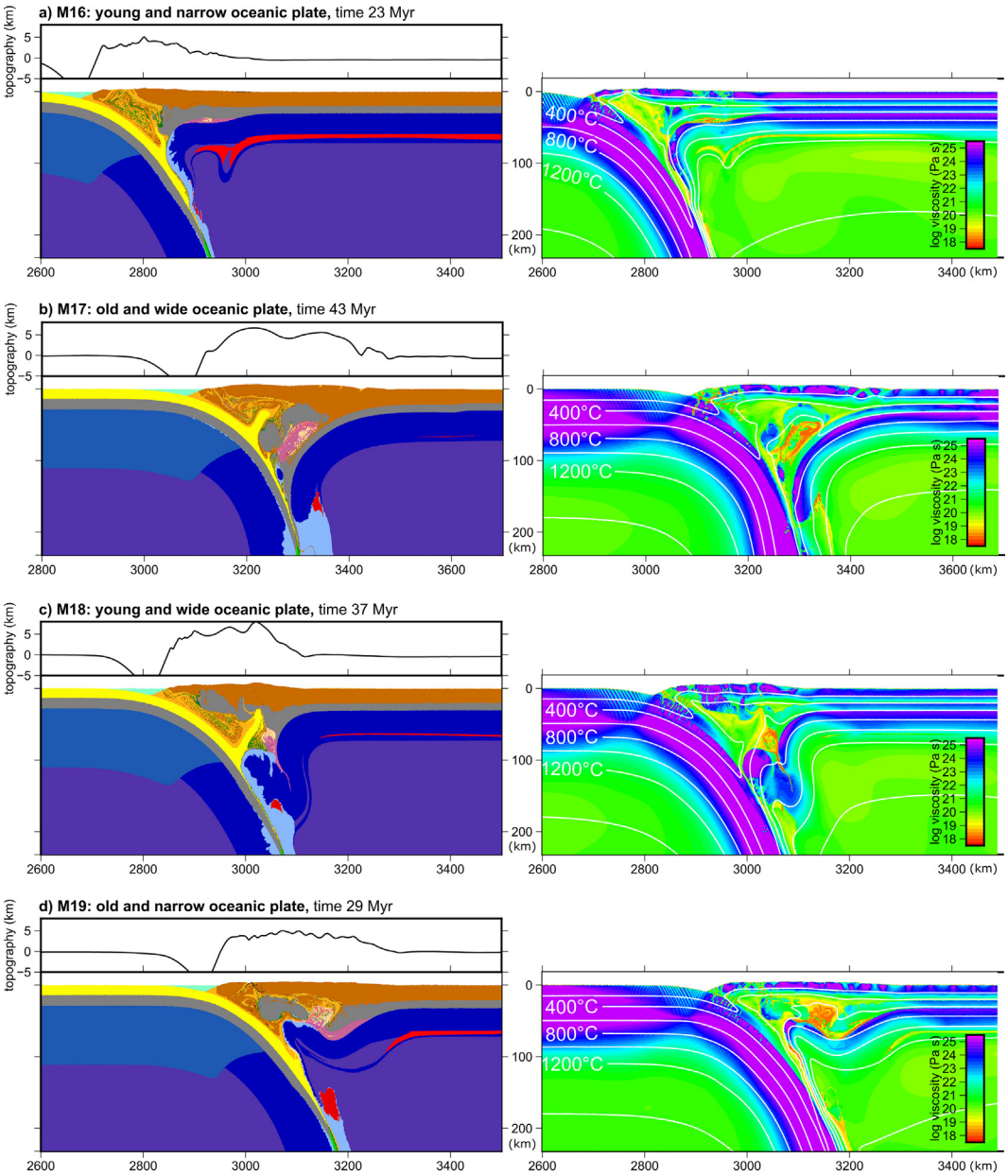

Fig. 12. Models M16-M19, which are characterized by combined variations in the initial age and width of the oceanic subducting plate: (a) a younger age (60 Myr) and a smaller width (500 km), (b) an older age (100 Myr) and a larger width (900 km), (c) a younger age (60 Myr) and a larger width (900 km), and (d) an older age (100 Myr) and a smaller width (500 km).

plate that is older (100 Myr) and narrower (500 km) does not cause relamination of the lower-plate felsic crust (model M19; Fig. 12d; Fig. S6), but the deformation of both the crust and lithospheric mantle of the upper plate extends over a greater distance, producing a broader (>300 km), more uniform, but less elevated (<6 km) orogen (Table 4; Fig. S1h).

5. Forward gravity modelling

5.1. Numerical method and models setup

The forward gravity models have been computed by using the distribution of density values at the Cartesian coordinates for each 2D numerical simulation (Fig. S7). For this purpose, we constructed rectangular prisms with the center coincident to each grid point of the numerical models and length and height equal to the internode spacing. The prisms width, along the third dimension (normal to the 2D model plane) was set to 5000 km, approximating an infinite plane with no density change occurring normal to the 2D section. It should be noted that this infinite extension can always be expected to result in larger anomalies with respect to a real-world scenario, where geological bodies have a finite size normal to the section. We computed the gravity effect of the models using the Cartesian prisms routines in Tesseroids software (Uieda et al., 2016). In order to ensure that the gravity effect is always computed outside of the model volume, the observation height was set to 10 km above the reference sea level. Furthermore, we excluded from the computation the prisms corresponding to the sticky air layer (1 kg m^{-3}).

Variations in topography have a large density contrast with respect to air. Therefore, they dominate the resulting gravity signal – similar to real-world "free air" gravity anomalies, which to some extent correlate with topography (Kirby, 2014; Pivetta and Braitenberg, 2020). In order to separate these effects and unmask those of the subsurface mass change, we implemented the gravity reduction of topography to obtain a Bouguer (BG) field. To this aim, we computed and removed the gravity signal produced by all the prisms above the model sea level. To reproduce a real-world terrain correction, which is customarily done with a constant density of above-sea-level masses (Hinze, 2003), we also tested the effect of replacing the actual density of the above-sea-level prisms with the conventional value of 2670 kg m^{-3}. By doing so, we isolated the effect of omitting the density deviations from 2670 kg m^{-3}, which would be mostly unknown when observing real data. Using the actual higher densities of the modelled crustal structures resulted in a more negative BG underneath areas of high topography (up to 30–50 mGal, around 20 % of the total BG anomaly).

Furthermore, computing the gravitational attraction of the model masses, without removing a reference model, results in an unwieldly absolute quantity. Hence, an anomalous gravity quantity is required, expressed as the difference with respect to a reference model (Maddaloni et al., 2022). In order to obtain such an anomaly, we computed the effect of a model with the same volume (i.e. the same 2D section extents and the same extension along the third dimension) and a 1D depth-wise variation in density (a reference density profile). This reference profile has been computed according to the average vertical density distribution in the rightmost 200 km of each cross-section, corresponding to the portion of the overriding plate negligibly influenced by the variations of the mass distributions, occurred during the continental collision. We can notice that the curves of reference density-depth distributions are almost overlapped, reflecting the trend given by the initial densities assigned to the layers composing the overriding plate (Fig. S8).

5.2. Results of the forward gravity models

The obtained BG anomalies (Fig. 13) are predominantly negative, reaching minimum values between −325.2 and −604.2 mGal, which are in good agreement with the corresponding maximum topographic elevations (Table 4). The minima of the BG anomalies tend to move towards the internal part of the orogen and become more pronounced with increasing width of the oceanic plate (Fig. 13b and 13 h), while they reach the maximum absolute value (−604 mGal) in the case of a smaller thickness (55 km) of the overriding plate (model M10; Fig. 10c). The spatial distributions of the modelled BG anomalies across the collision zone (Fig. 13) also correlate well with the topography (Fig. S1) and Moho depth (Fig. S2), as also evidenced by the strongly negative values of the statistical correlation coefficient (Table S1). In particular, the absolute values of the correlation coefficient of the BG anomalies with topography and Moho depth are always above 0.85 (Table S1), except for the experiment with a thicker (65 km) overriding lithosphere (model M11; Fig. 10d). Importantly, apart from surface topography and Moho depth, the distribution and amount of relaminated material in the overriding plate also has a strong influence on the resulting pattern of modelled BG anomalies (compare Fig. 13 and the compositional fields in Figs. 7–12).

The shape of the BG anomalies around their minima varies between models, in agreement with the lateral extent of the low values, determined as the distance between the two farthest points falling in the lowest 10 % of the distribution. Indeed, such a distance is the shortest in the models characterized by a well-defined minimum underlain narrow orogens (model M2, M7 and M8, Fig. 13a-c, Figs. S1–S2, Table 4) and the largest in the models having a less-defined minimum, underlain wide orogens (model M1, M5, M10, M14, M17, M19, Fig. 13a, 13d, 13f-h, Figs. S1-S2, Table 4). With increasing distance from the trench, the influence of the subduction and collision processes on the compositional fields (Figs. 7–12, left column) and the resulting density distributions (Fig. S7) tends to decrease, so that the corresponding negative anomalies reduce accordingly and even become weakly positive near the edges of the modelled area (Fig. 13).

Compared to the modelled BG anomalies (Fig. 13), the BG anomalies observed along the Zagros cross-sections (Fig. 4) are characterized by a smaller range between minimum and maximum values (from −90 mGal to 100 mGal), which can be explained by a higher topography and a greater thickness of the crust in the modelled collision zone (Figs. 7–12) than the observed relief and the Moho depth estimated from seismic data (Fig. 2). However, the pattern of several modelled BG anomalies with a well-defined minimum, localized in the external part of the orogen, is similar to that observed along transect B-B', which crosses the central sector of the Zagros (Fig. 4b). In particular, we refer to the models with a different oceanic age (models M3 and M5; Fig. 8b,d), a larger width (model M7; Fig. 9b), a different convergence rate (models M8 and M9; Fig. 10a-b), a thicker subducting continental plate (model M12; Fig. 11a), and a greater thickness of subducting felsic crust (model M13; Fig. 11b) compared to the reference values (model M1; Fig. 7). On the contrary, the BG anomaly pattern derived from the reference model M1 (Fig. 7) as well as from the experiments with a thicker overriding plate (model M11; Fig. 10d), a weak subducting lower crust (model M14; Fig. 11c), a thinned continental margin (model M15; Fig. 11d), and a combination of an older and narrower oceanic subducting plate (model M19; Fig. 12d) are more similar to the trend of transect A-A' crossing the northwestern sector of the Zagros (Fig. 4a), where the highest negative values are more widely distributed along the central part of the orogen. The only models that show a pattern characterized by a minimum located in the internal part of the orogen, and thus different from both transects, are those obtained in the

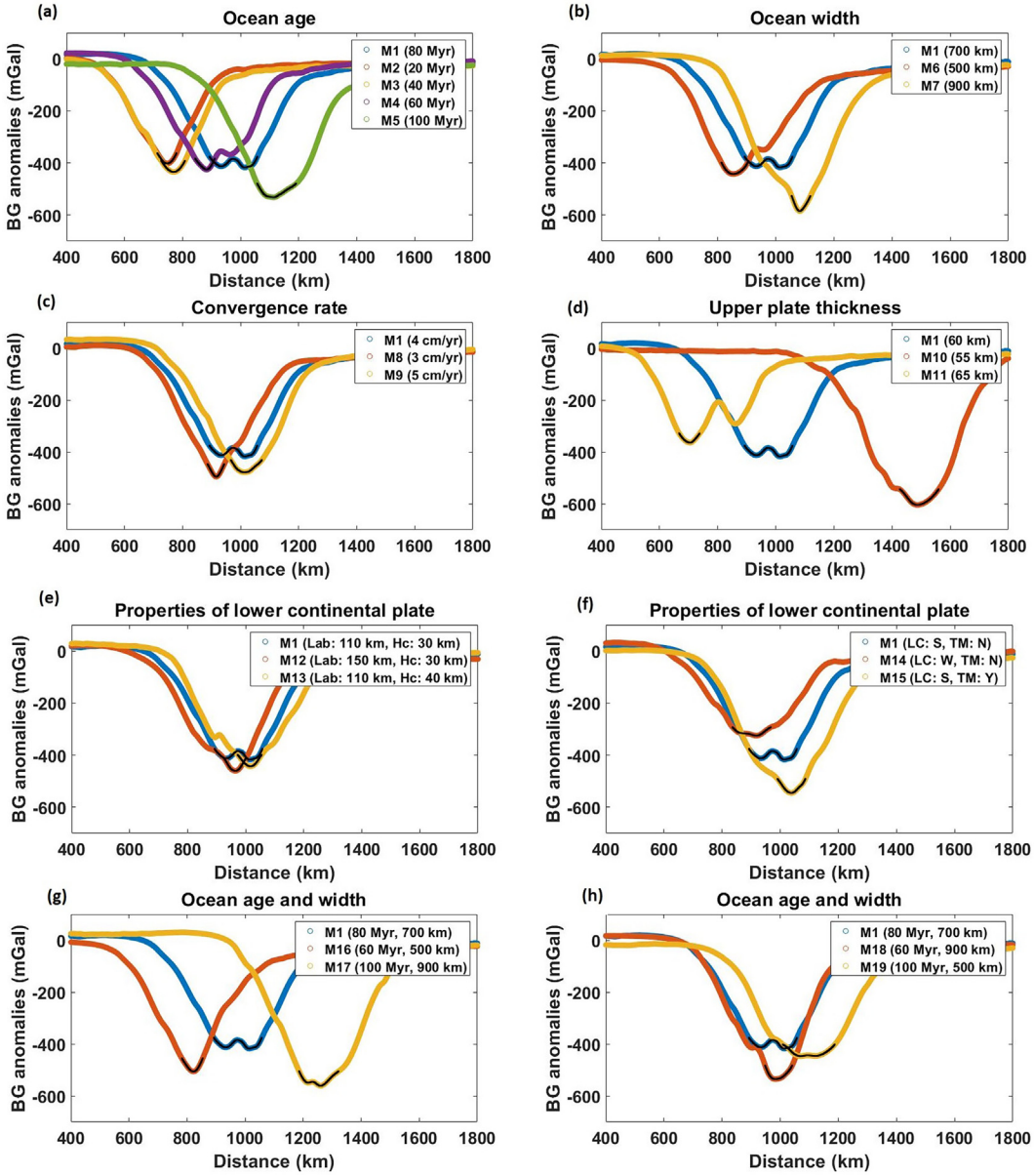

Fig. 13. Modelled Bouguer (BG) anomalies, which are calculated from the density distributions of the thermo-mechanical experiments M1-M19 (Fig. S7), grouped by variations in (a) initial oceanic age (models M2-M5), (b) initial oceanic width (models M6-M7), (c) convergence rate (models M8-M9), (d) overriding plate thickness (models M10-M11), (e-f) properties of the continental part of the subducting plate (models M12-M15), and (g-h) combined effects of oceanic plate age and width (models M16-M19): lithospheric and upper crustal thickness (e), rheology of the lower crust and presence of a thinned continental margin (f), and age and width of the oceanic plate (g-h). Reference model M1 is shown in all panels. Thin black lines indicate the sectors falling in the lowest 10% of the distribution. Abbreviations in the legends: Lab – Lithosphere-asthenosphere boundary; Hc – Crustal thickness; LC – Lower crust; S – Strong; W – weak; TM – Thin margin; N – No; Y – Yes. A similar grouping of experiments is used in Figs. S1-S3.

experiments characterized by a thinner overriding plate (model M10; Fig. 10c) and a combination of a younger and wider oceanic plate (model M18; Fig. 12c).

6. Discussion

6.1. Timing of the Zagros orogen building and convergence rates in models and nature

In the performed thermo-mechanical models, the formation of the orogen occurs mainly during the continental collision after a preceding phase of oceanic subduction. Each numerical simulation lasts between 24.0 Myr (the shortest run in model M18) and 43.1 Myr (the longest run in model M19), ending when the tip of the subducting continent reaches a depth of ~ 200 km. The duration of the model thus increases (decreases) with increasing (decreasing) age and width and decreasing (increasing) velocity of the subducting oceanic plate (models M1-M9) as well as with decreasing (increasing) stiffness (thermal thickness) of the overriding plate (models M10-M11). As the main phase of mountain building starts with the entry of the continental margin into the trench, the formation of the modelled orogen generally takes ~ 10 Myr (see evolution of reference model M1; Fig. 7).

The onset of continental collision in the Zagros Collision Zone occurred in the Late Eocene-Early Oligocene (~30–35 Ma), whereas the major deformation phases that mainly formed the Zagros orogen ended at ~ 10 Ma (e.g., Agard et al., 2011; Ballato et al., 2011; Darin and Umhoefer, 2022). This apparent discrepancy with

modelling can be explained by the long-lasting (~15 Myr) phase of so-called "soft collision" (e.g., Agard et al., 2011; Ballato et al., 2011; Madanipour et al., 2017; Darin and Umhoefer, 2022), when collisional deformation was very limited, but led to a rapid reduction in convergence velocity (e.g., Boutoux et al., 2021). Our experiment with reduced thermal thickness at the passive continental margin (model M15) confirms that the initial subduction of the thinned continental lithosphere does not contribute significantly to the formation of the orogen (Fig. S4) and does not have a major impact on the resulting extent of crustal relamination (Fig. 11d). In the latest Oligocene to middle Miocene (~25–12 Ma), the "soft collision" switched to the "hard collision" stage, which is characterized by accelerated regional deformation (Agard et al., 2011), reflected in rapid crustal thickening, surface uplift, and rock exhumation (e.g., Boutoux et al., 2021; Mouthereau et al., 2012). This transition from "soft" to "hard" collision is also marked by a change in the composition of volcanic products along the UDMA from predominantly calc-alkaline to K-alkaline (e.g., Rabiee et al., 2020), while the initial emplacement of adakites becomes progressively younger from NW (~27–22 Ma) to SE (~7 Ma) (Chiu et al., 2013), consistent with along-strike diachroneity of Zagros collision and orogeny (Darin and Umhoefer, 2022). Indeed, these rocks were formed during the last phase of arc magmatism, likely as a result of initial crustal thickening and lithospheric delamination, which is a consequence of the"hard collision" with the Arabian plate. To summarize, the main formation of the Zagros orogen lasted on average ~ 10 Myr after the onset of the "hard" continental collision, which agrees with our numerical results.

In our models, we have assumed rates of plate convergence, that are varied in different experiments (3–5 cm yr^{-1}), corresponding to the range of estimates from geological observations (e.g., Boutoux et al., 2021). In contrast to our simulations, where the applied velocity remains constant during the evolution of the system, the natural convergence velocities demonstrate an oscillatory pattern with a period of ~ 15–20 Myr. In particular, there were two periods of relatively low subduction rates (~2 cm yr^{-1}) at ~ 75–55 Ma and ~ 25–5 Ma and two periods of relatively high subduction rates, with a peak convergence velocity of ~ 5–6 cm yr^{-1} at ~ 75 Ma and at ~ 55–35 Ma (Boutoux et al., 2021). This oscillatory trend in velocity nearly coincides with pronounced episodes of contraction and extension within the upper plate. In particular, two episodes of back-arc extension, from ~ 100 and ~ 80 Ma and from ~ 40 to ~ 60 Ma, and two episodes of compression, from ~ 70 to ~ 55 Ma and from ~ 35 Ma to present, have been recognized and interpreted as effects of slab retreat and advance, respectively (Boutoux et al., 2021). The last episode of compression was induced by the closure of the Neo-Tethys ocean when the Arabian continental plate intruded into the trench, resulting in a significant reduction of the subduction velocity to ~ 1.5–2.0 cm yr^{-1} (e.g., Boutoux et al., 2021). According to our experiments, an increase in the convergence rate generally reduces the extent of felsic relamination, as the subducting crust is in contact with warm material for a shorter time in this case (Fig. 10b). However, differences in the internal structure of the orogen (Fig. 10a-b), which are caused by relatively small variations in convergence rates (from 3 to 5 cm yr^{-1}), do not have a noticeable effect on its overall shape (Fig. S1c).

6.2. Observed and modelled internal structure and surface shape of the orogen

The detailed geophysical model for the central part of the Zagros Collision Zone reveals an unusual structural inversion, where the stretched mafic crust forming the shallow part of the Iranian plate is underlain by the relaminated crust of the subducting Arabian plate, which consists of a felsic and mafic layer (Talebi et al., 2020). Accordingly, another crustal-scale seismic imaging (Dashti et al., 2020) shows that at least 7–9 km of high-density rocks of the middle/lower crust were brought to shallow depths at the collision margin of the overriding continent.

Similar crustal structures, characterized by the mafic layer of the overriding plate being sandwiched between two felsic layers, are reproduced in several of our experiments, in which the lower-plate relaminant intrudes between the upper-plate lithospheric mantle and the lower crust, that was subjected to extension and even boudinage during the preceding oceanic subduction (see e.g. reference model M1; Fig. 7). Such a crustal configuration may generate a trend of BG anomalies characterized by a relatively broad minimum area with two local minima, similar to that observed along transect A-A′ (e.g., reference model M1; Fig. 13). Apart from the reference model M1, this style of *syn*-collisional crustal relamination is detected in the experiments with a younger and wider oceanic plate (models M4, M7, and M18; Fig. 8b, 9b, and 12c), a thinner overriding plate (model M10; Fig. 10c), a thicker continental subducting plate (model M12; Fig. 11a), and in the presence of a thinner continental margin (model M15; Fig. 11d). Alternatively, the relaminated material appears to (1) overthrust the lower crust of the overriding lithosphere in the experiments with the youngest oceanic ages (models M2 and M3; Fig. 8a-b), different convergence rates (models M8 and M9; Fig. 10a-b), and a combination of an older and wider oceanic plate (model 17; Fig. 12b) or (2) push mafic boudins in a horizontal direction towards the interior of the overriding plate in the experiments, in which continental lithosphere of the subducting plate is characterized by thicker upper crust (model M13; Fig. 11b) and weak lower crust (model M14; Fig. 11c). In the remaining experiments, such as those with an older and narrower oceanic plate (models M5, M6, and M19; Fig. 8d, 9a, and 12d), a thicker overriding plate (model M11; Fig. 10d), and a combination of a younger and narrower oceanic plate (model M16; Fig. 12a), most of the felsic material remains attached to the subducting plate, so that crustal relamination does not occur or occurs only to a very small extent.

Despite the differences between the crustal models suggested by the interpretation of the geophysical data (see Section 3.1), there is a general agreement between the latest studies (Kaviani et al., 2020; Irandoust et al., 2022) that in the central Zagros the position of the highest topography in the ZFTB is shifted with respect to the abrupt deepening of the Moho below the SSZ. In contrast, in the northern part of the orogeny, the elevated topography is more evenly distributed across the collision zone, showing a higher correlation with crustal thickness (Table 1), which is also more uniform and not subject to strong fluctuations.

In our experiments, the resulting width of the orogen (Table 4) varies between 170 km (model M11; Fig. 10d; Fig. S1d) and 377 km (model M10; Fig. 10c; Fig. S1d), while its maximum height covers the range between 5.1 km (model M2; Fig. 8a; Fig. S1a) and 9.1 km (model M10; Fig. 10c; Fig. S1d). The orogen becomes systematically wider with increasing initial age of the oceanic plate (Table 4), as shown by models M2-M5 (Fig. 8; Fig. S1a) and M16-M19 (Fig. 12; Fig. S1g-h). The maximum height also follows the same trend (i.e. increasing in value with aging of the oceanic lithosphere; see Table 4), although a relatively narrow (~250 km) orogen in model M18, that combines a young age of the plate with its large original width (Fig. 12c), paradoxically has the second highest topography (8.2 km; Fig. S1h), which is only lower than in the case of a reduced thickness of the overriding plate (model M10; Fig. 10c), where it reaches the above-mentioned absolute maximum of 9.1 km (Fig. S1d).

The deepest crustal roots, characterized by a Moho depth of $\geq$ 80 km (Fig. S2), and the low values (falling in the lowest 10 % of the distribution) of BG anomalies (Fig. 13), coincide with the external or central part of the orogen in most experiments,

where often the highest topography is observed (Fig. S1). Indeed, variations in Moho depth are strongly correlated with those in surface topography (Table S1). The best example of such a correlation is model M10 (Table 4), where a thinner overriding plate (Fig. 10c) generates the broadest and most elevated orogen, together with the widest (>200 km) deep crustal roots (Fig. S2d) and the most pronounced (−604.2 mGal) BG anomaly (Fig. 13d). Similar to the trend of orogenic lateral extent (see above), the width of the deep crustal roots also increases with the age of the oceanic plate (models M2-M5; Fig. 8; Fig. S2a), while the narrowest deep crustal roots (<60 km; Table 4) are detected in the experiments with a smaller width of the original oceanic plate (model M6, M16, and M19; Fig. 9a, 12a,d; Fig. S2b,g-h), a thicker (stiffer) overriding plate (model M11; Fig. 10d; Fig. S2d), and a rheologically weaker subducting crust (model M14; Fig. 11c; Fig. S2f).

In addition to the correlation between the topography and the distribution of the Moho depth (Table S1), which is also reflected in the correspondence between the resulting width of the orogen and the deep crustal roots (Table 4), the behaviour of the surface topography is related to the internal structure and composition of the crust in the different parts of the orogen. In particular, short-wavelength undulations are typical of the topography above a felsic relaminant and sedimentary mélange, whereas long-scale topography variations are indicative of mechanical coupling between the upper crust and mantle lithosphere by a rheologically strong mafic lower crust (Burov, 2011; Koptev et al., 2019), as can be clearly seen from the comparison of experiments with the youngest (model M2; Fig. 8a) and oldest (model M5; Fig. 8b) subducting ocean (Fig. S1a). The observed changes in the topographic length scales across and along the orogen (see Section 3.1) can, therefore, be attributed to variations in the composition of the crust, with the relative distribution of relaminated felsic material and mafic blocks of the lower crust playing the decisive role. As illustrated by the evolution of reference model M1 (Fig. 7), the lower crust of the overlying plate undergoes intense extension during the early phase of ocean-continent subduction, leading to segmentation of the originally coherent mafic layer into isolated blocks (or boudins), which may subsequently be underlain by relaminated material and pushed upwards to extremely shallow levels (see e.g. model M7; Fig. 9b). Furthermore, relaminated felsic crust and sedimentary mélange can flow horizontally within the overriding plate and fill the space between the separated mafic boudins, resulting in a lateral decrease in viscosity and deepening of the Moho from the external to the central part of the orogen, which corresponds to the transition from a strong uplifted block to a weak intruded material (see models M1, M7, M12, M15, M18, and M19; Fig. 7e, 9b, 11d, and 12c-d). Indeed, the thickening of the crust could be the response to horizontal compression, similar to that in an incompressible hydraulic fluid (e.g., Paul et al., 2006). A sudden reduction in the number of earthquakes, accompanied by a smoothing of the surface topography and an increase in Moho depth across the collision zone (especially in the central sector of the orogen, from the ZFTB to the SSZ), may, therefore, be explained by the rapid decrease in mechanical strength due to the lateral alternation between high-viscosity (mafic boudins) and low-viscosity (felsic relaminant) compositional units of the orogen. It is also important to note that during crustal thickening, when temperatures near the Moho reach ~800 °C, the lowermost part of the rheologically strong mafic crust is subject to partial melting, causing the effective viscosity to drop abruptly (see, for example, the broadly molten crustal roots in model M10; Fig. 10c). Most of the melting of the lower crust (if any) always takes place in the internal part of the orogen, since in the external part, near the subduction zone, the temperatures are not high enough to induce melt formation (Figs. 7–12).

As for the lithospheric mantle of the upper plate below the collision zone, in most experiments it is not only locally hydrated and partially molten, but also strongly deformed and buckled (Figs. 7–12) due to the compressive stresses caused by the continuous convergence between the plates (Fig. 6). The resulting total thickness of the overriding lithosphere beneath the orogen is typically ~ 150 km, that is in apparent contradiction to the thin Iranian plate (<100 km) from the interpretation of seismic tomography data (Koulakov, 2011; Schaeffer and Lebedev, 2013; Talebi et al., 2020; Veisi et al., 2021). This is a consequence of the lack of processes in our modelling, which are related to the rupture slab of the subducting slab (see Section 7). The last slab break-off event occurred after the main phase of the Zagros formation in the Late Miocene (Agard et al., 2011) and caused the upward flow of asthenospheric material through the slab window, significantly reducing the thickness of the overlying lithospheric mantle and thus masking the effects of *syn*-collisional buckling and thickening. These processes have particularly affected the UDMA, composing the internal part of the Zagros orogen, which is characterized by a thin and hot lithosphere (e.g., Talebi et al., 2020; Mohammadi et al., 2022).

6.3. Main cause of along-strike structural variations in the Zagros orogen: Heterogeneity of colliding plates or obliquity of the Neo-Tethys closure?

The different trends in Moho depth and topography along the two cross-sections through the Zagros orogen described above (see Section 3) clearly show along-strike transition from a broader to a narrower deformation zone in the northwestern (transect A-A') and central (transect B-B') segments, respectively (Fig. 2).

The shape of the orogens is mainly determined by the amount and spatial distribution of shortening, which in turn depends on the stiffness of the lower and upper plates (e.g., Gao et al., 2023). The phases of compression and extension that occurred during the subduction of the Neo-Tethys ocean may have led to varying degrees of weakening and thinning of the Iranian lithosphere, making, for example, the northern sector of the Zagros more susceptible to deformation during the collision. Therefore, the original differences in the properties of the colliding continents along the future Zagros could be the main reason for the resulting structural differences between its northwestern and central segments. To investigate the role of these heterogeneities, we performed experiments with variable properties for both the overriding and subducting continental lithosphere (models M10-M15).

Variations in different parameters that control the composition and rheological structure of the subducting continent (models M12-M15) lead to pronounced differences in the style and extent of intra-continental relamination and thus the internal structure of the resulting orogen (Fig. 11). However, the modelled widths of the orogens and their maximum heights are close to each other in all these experiments (models M12-M15) and also to the values of the reference model M1 (Table 4).

In contrast, changes in the thermal thickness (and hence integrated strength) of the overriding continental plate (models M10-M11) appear to have a much stronger effect on the width of the area subject to compressive deformation, and thus on the lateral extent of the emerging orogen. In particular, with the weakening of the overriding lithosphere, which is achieved by reducing its initial thickness by only 5 km (model M10), the inward propagation of ductile deformation and the partial melting of the deep mafic crust becomes much more pronounced (Fig. 10c), compared to the reference model M1 (Fig. 7e). This is also reflected in a clear broadening of the resulting orogen (the final width is > 350 km), which is also characterized by the highest value of topography (9.1 km) ever achieved in our experiments (Table 4; Fig. S1d). Such

a trend of the relief is similar to that along the northwestern transect A-A' (Fig. 4a), where the elevated topography (~1.5 km) extends over a distance of ~ 550 km and reaches the highest peak (>3 km) in the Alborz mountains, in line with the maximum of the modelled height located in the most internal part of the orogen, as a result of long-distance propagation of compressional deformation in a weak overriding plate (Fig. 10c). We, therefore, argue that the high topography of the Alborz mountains can be mainly due to the widespread collisional deformation in the weak upper plate, while the potential effect of upwelling asthenospheric flow producing dynamic topography (e.g, Mohammadi et al., 2013) is likely of secondary importance.

On the other hand, the thickening of the continental lithosphere by the same value of 5 km (model M11) has the opposite effect. The associated increase in upper plate stiffness, mimicking a relatively stronger tectonic micro-blocks in the Central Iran (Motaghi et al., 2017), leads to an extreme localization of deformation near the trench (Fig. 10d), with the consequent formation of a very narrow (170 km) orogen (Table 4; Fig. S1d) that resembles the asymmetric topography along the central transect B-B' (Fig. 4b). However, despite the similarities in the observed and experimental topography, the model M11 does not reproduce the relamination of felsic material from the subducting Arabian plate into the crust of the overlying Iranian plate, which has been clearly demonstrated by detailed seismic tomography in the central Zagros (Talebi et al., 2020). In contrast, the anomalously thick crust (uncut Moho depth is > 100 km) beneath the modelled narrow orogen consists mainly of a massive intrusion of the lithospheric mantle (Fig. 10d), a peculiar structure that is not reproduced in any of the other experiments and is not detected in the geophysical data. In addition, the synthetic BG anomaly obtained from the density distribution of model M11 shows more widely distributed lowermost values with two local minima (Fig. 13d) than those observed along transect B-B' (Fig. 4b). We conclude, therefore, that the reference value for the thickness of the overriding lithosphere (60 km) better fits the thermo-rheological properties of the Iranian plate in the central part of the Zagros, as it allows to prevent the outward propagation of deformation from the collision zone while ensuring a sufficient volume of relaminated felsic crust in the upper plate (see e.g. reference model M1; Fig. 7).

Since the variations in the properties of the colliding plates do not adequately capture the observed structural changes along the Zagros orogen, we also investigated the effects of the oblique closure of the ocean between Arabia and Eurasia by testing different combinations of the age and original lateral extent of the oceanic lithosphere, separating the continents at the beginning of our experiments (models M16-M19). In particular, experiment M19, characterized by an older and narrower ocean (Fig. 12d; Fig. S6), and model M18, where in contrast the oceanic plate is younger and wider (Fig. 12c; Fig. S5), roughly correspond to the northwestern and central segments of the Neo-Tethys ocean at ~ 60 Ma (Fig. 14a), when its subduction beneath the southern margin of the Iranian plate had just re-initiated after the slab break-off event (Agard et al., 2011). Indeed, from NW to SE, the oceanic floor of the Neo-Tethys became progressively younger and its width increased (e.g., Seton et al., 2012), as reflected by a strong diachroneity of subsequent collision and orogeny (e.g., Darin and Umhoefer, 2022).

The resulting topography in model M18 (Fig. 12c), which corresponds to the conditions in the central Zagros section (younger and wider subducting ocean), reproduces not only the narrower orogen (~250 km instead of > 300 km in reference model M1), but also the significantly higher maximum altitude (8.2 km instead of 7.3 km), which is, however, shifted towards the internal part of the orogen (Fig. S1h). In contrast to model M11, in which the proper intracrustal relamination is not reproduced (Fig. 10d), the relatively narrow orogen of model M18 is underlain by felsic material that has detached from the subducting slab and intruded between the lower crust and the lithospheric mantle of the overlying plate. It is also important to note that in contrast to reference model M1, where the upper-plate lower crust is divided into several blocks

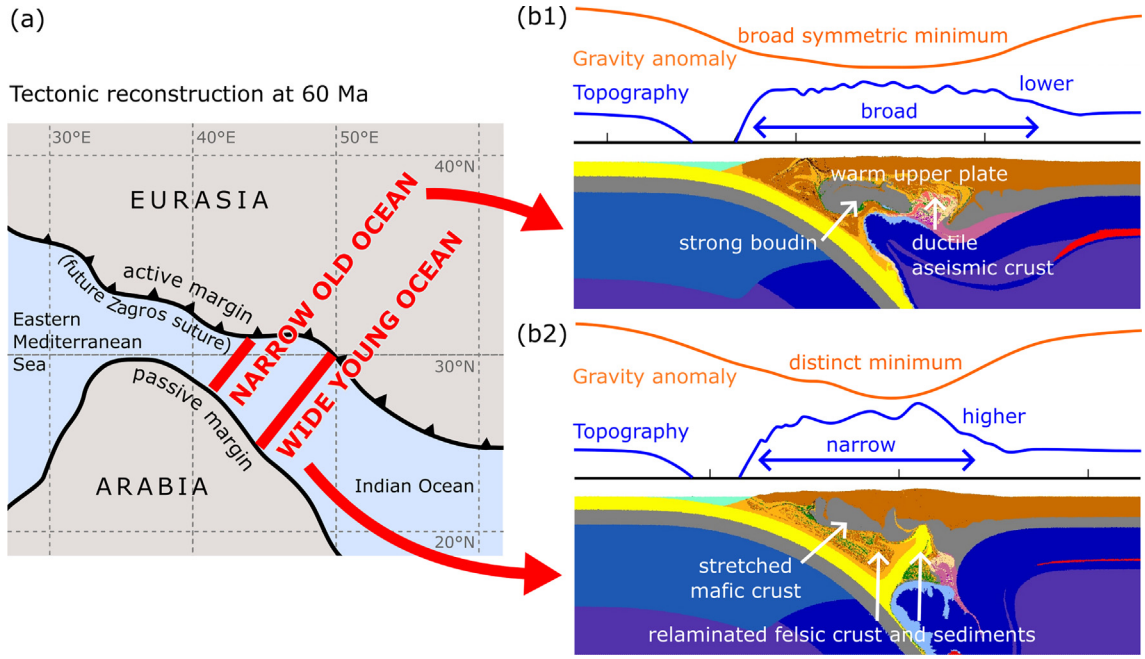

Fig. 14. Effects of obliquity of the Neo-Tethys closure on variations in internal structure and surface topography along the Zagros orogen. (a) Plate reconstruction at ~ 60 Ma showing a progressive increase in the width of the Neo-Tethys ocean from NW to SE, that led to a strong diachroneity in the subsequent processes of continental collision and orogeny (modified after Darin and Umhoefer, 2022). The positions of the transects defining the initial configurations for the corresponding numerical models are shown by black solid lines. (b) Thermo-mechanical experiments M18 and M19, in which the oceanic subducting plate is (b1) a younger and wider (central transect B-B') and (b2) an older and narrower (northwestern transect A-A') than in the reference case M1. The transition from a narrower and higher orogen in model M18 (panel "b1") to a broader and lower orogen in model 19 (panel "b2") fits with the observations (see Fig. 2) and argues for the key role of collisional obliquity in the along-strike differences in the present-day structure of the Zagros Collision Zone.

(boudins) with lower-plate relaminant flowing between them (Fig. 7e), model M18 shows a continuous yet stretched mafic layer (Fig. 12c), in agreement with the interpretation of detailed seismic tomography in the central Zagros (Talebi et al., 2020).

The experiment with the older and narrower oceanic plate (model M19), which mimics conditions in the northwestern segment of the Zagros, yields a much more uniform and broader (325 km) yet less elevated (5.8 km) orogen (Fig. S1h), consistent with observations along the corresponding transect (cross-section A-A'; Fig. 4a). Although relamination of the felsic upper crust does not occur in this experiment, the space between the mafic boudins of the overriding plate is filled with sedimentary mélange scraped from the oceanic plate (Fig. 12d). Together with the partial melting of the lowermost mafic crust, the presence of this sedimentary mélange causes an abrupt drop in effective viscosity (Fig. 12d, right column), which is consistent with the observed sharp decline in seismic activity across the orogen (Fig. 2).

In summary, our study confirms the importance of heterogeneities in the collided plates for the style and extent of the relamination and the shape of the orogen (models M10-M15), so that they should be investigated in more detail in future modelling studies (see Section 7). However, the experiments with the original ages and sizes of the subducting oceanic domain, whose variations roughly mimic the Neo-Tethys configuration at the time of the penultimate slab break-off (models M18-M19), better reproduce the geophysical data and geomorphologic patterns in the corresponding segments of the Zagros Collision Zone (Fig. 14b). Therefore, we argue that the obliquity of the continental collision between Arabia and Eurasia is the main cause of the observed variations in crustal architecture and topographic features along the Zagros orogen.

7. Model limitations and future perspectives

The 2D modelling approach adopted in this study naturally omits the 3D effects associated with oblique subduction (Malatesta et al., 2013, 2016), including a gradual transition from oceanic to continental subduction (Li et al., 2013; Sternai et al., 2014; Menant et al., 2016), with a consequent laterally variable convergence velocity. Along-strike differences in trench advance or retreat are known to produce laterally variable patterns of upper plate deformation, sedimentation, and mantle flow (Balázs et al., 2021; Andrić-Tomašević et al., 2023), which, together with far-field tectonics and climatic events, have contributed to broaden the Zagros orogen, forming its present-day shape. By changing the corresponding parameters of our 2D models, we have attempted to capture along-orogen variations in the initial conditions and reproduce the observed orogen shape and crustal structures in different segments of the Zagros. In the future, however, true 3D experiments that incorporate and generate these lateral heterogeneities in a self-consistent manner are needed.

In our models, we assume a constant convergence rate, that varies between 3 and 5 cm yr^{-1} in different experiments. Although these values fit well with estimates for the pre-collision phase of system evolution (Boutoux et al., 2021), a slower relative motion of $\sim$ 2 cm yr^{-1}, currently observed by GPS data (Vernant et al., 2004; Khorrami et al., 2019), is known to have been established since the "hard collision" between the Arabian and Iranian plates in the Late Oligocene to Middle Miocene (Darin and Umhoefer, 2022). The reduction in the convergence rate during and after collision can have far-reaching consequences, leading to slab deformation, steepening, and even break-off (e.g., Agard et al., 2011), processes that could have caused vigorous small scale convection with associated thinning of the upper plate and thus need to be considered in future models of the Zagros orogeny. Particular attention should be paid to the opening of intra-slab windows and the resulting asthenospheric inflow at the subcrustal level (e.g., Duretz et al., 2011), which may have a significant impact on the spatial and temporal distribution of magmatic products (e.g., Rabiee et al., 2022).

Finally, the effects of inherited and acquired heterogeneities in the Arabian and Indian plates were only superficially investigated in our study, although they may play a significant role in shaping tectonic structures (e.g., Perron et al., 2018). In particular, tectonic deformation zones inherited from the collision of Iranian plate micro-blocks and from the earlier Gondwana assembly, and developed through multiple compression/extension phases during the Neo-Tethys subduction (Boutoux et al., 2021) should be included as compositionally distinct units in future 2D and 3D numerical studies. The effects of pre-collisional magmatism are also important, as numerous intrusions emplaced during the extensional phases of the upper plate may have thickened the crust of the overriding plate already before the collision, contributing in part to the formation of the orogen (e.g., Paul et al., 2006).

8. Conclusions

In this study, we investigate the structure of the crust and lithospheric mantle in the Zagros Collision Zone using recently acquired geophysical data and apply geodynamic numerical modelling to understand the effects of the properties of the colliding plates and the obliquity of the Neo-Tethys closure on the resulting shape and internal configuration of the orogen.

As evidenced from observations, the northwestern sector of the Zagros orogen is characterized by a fairly uniform increase in Moho depth and a symmetric surface topography. On the contrary, in the central part of the Zagros, a lower dip angle and a greater indentation of the Arabian plate lead to an abrupt crustal thickening accompanied by a rapid transition from an elevated to a smoothed relief and a sharp decrease in seismicity, probably due to a viscosity reduction in the overriding Iranian plate.

In order to understand the reason for these along-strike variations, a series of 2D thermo-mechanical experiments were carried out considering initial and boundary conditions relevant to the study area. The control parameters (age and width of initial oceanic domain, convergence rate, specific properties of subducting continental lithosphere, and thickness of overriding plate) were varied within the range of uncertainties and accounting for their possible lateral changes, due to along-strike heterogeneities of the colliding plates and the oblique closure of the Neo-Tethys ocean. Based on the results of the numerical models and their comparison with the observed data, we can draw the following conclusions:

1 After the switch from ocean-continent subduction to continent–continent subduction/collision, the continental crust of the overriding plate thickens considerably (up to 80 km). Such thickening might not only be a consequence of mechanical shortening, accommodating continuous convergence, but also a result of so-called "crustal relamination", when crustal material from the lower plate is emplaced (relaminated) at the base or within the crust of the upper plate. This is consistent with the vertical alternation of felsic and mafic crustal layers recently discovered in the central Zagros by regional seismic tomography. In agreement with earlier numerical studies, a thin ($\leq$60 km) lithosphere of the upper plate is the key characteristic that allows profound relamination into its crust and formation of a wide orogen.

2 In certain experiments, the boudinage of the lower crust during the pre-collisional extension of the overriding plate leads to the formation of isolated felsic and mafic blocks that control the spatial transitions between short- and long-wavelength surface topography.
3 The combination of thermo-mechanical and forward gravity modelling approaches reveals a large influence of the amount and distribution of relaminated material on the geophysical signal of the orogen, such as the lateral trends of Bouguer gravity anomalies.
4 The relatively low seismic activity in the Iranian plate can be attributed not only to its thinning and weakening prior to collision, but also to *syn*-collisional relamination of felsic crust and sediments and partial melting in the lower crust, all of which significantly reduce the effective viscosity.
5 The internal structure of the collision zone and the surface shape of the orogen are determined by the degree and style of the relamination process, which in turn depends on the modelling parameters, controlling not only the properties of the colliding continents but also the oceanic lithosphere between them. Especially, in the experiments with an old and narrow subducting oceanic plate, a broad and relatively low plateau is obtained, whereas a young and wide slab tends to form a narrow and a more elevated orogen. Such a trend is consistent with the progressive closure of the Neo-Tethys from NW to SE: in the northwestern part of the Zagros (where the paleo-ocean was originally narrower) the present-day orogen is broader, while the central Zagros (where the oceanic part of the Arabian plate was wider) is asymmetric and high.

Magdala Tesauro: Investigation, Conceptualization, Methodology, Validation, Data Curation, Writing – Original Draft, Writing – Review & Editing, Visualization.

Petra Maierová: Conceptualization, Methodology, Thermo-mechanical Models Software, Investigation, Visualization, Writing – Review & Editing.

Alxander Koptev: Conceptualization, Investigation, Writing – Review & Editing.

Alberto Pastorutti: Conceptualization, Methodology, Gravity Models Software, Investigation, Visualization, Writing – Review & Editing.

Tommaso Pivetta: Investigation, Review & Editing.

Ivan Koulakov: Seismic Tomography Software.

Carla Braitenberg: Methodology, Gravity Models Software, Review & Editing, Project coordination.

Declaration of competing interest

The authors declare that they have no known competing financial interests or personal relationships that could have appeared to influence the work reported in this paper.

Acknowledgements

This study is supported by the PRIN 2017 project '*Intraplate deformation, magmatism and topographic evolution of a diffuse collisional belt: Insights into the geodynamics of the Arabia-Eurasia collisional zones*' (MT, AP, TP, CB) and by project no. 23-08249S of the Czech Science Foundation (PM). We acknowledge Taras Gerya for providing the computer code used to generate our thermo-mechanical numerical models. We thank Paolo Ballato for useful references and two anonymous reviewers for valuable and constructive comments.

Appendix A. Supplementary data

Supplementary data to this article can be found online at https://doi.org/10.1016/j.gr.2024.06.009.

References

Agard, P., Omrani, J., Jolivet, L., Whitechurch, H., Vrielynck, B., Spakman, W., et al., 2011. Zagros orogeny: A subduction-dominated process. Geol. Mag. 148 (5–6), 692–725. https://doi.org/10.1017/S001675681100046X.

Amante, C., Eakins, B.W., 2009. ETOPO1 1 Arc-Minute Global Relief Model: Procedures. Data Sources and Analysis. NOAA Technical Memorandum NESDIS NGDC-24, 19 pp.

Andrić-Tomašević, N., Koptev, A., Maiti, G., Gerya, T., Ehlers, T.A., 2023. Slab tearing in non-collisional settings: insights from thermo-mechanical modelling of oblique subduction. Earth Planet. Sci. Lett. 610, 118097. https://doi.org/10.1016/j.epsl.2023.118097.

Artemieva, I.M., 2006. Global 1× 1 thermal model TC1 for the continental lithosphere: implications for lithosphere secular evolution. Tectonophysics 416 (1–4), 245–277. https://doi.org/10.1016/j.tecto.2005.11.022.

Ballato, P., Uba, C.E., Landgraf, A., Strecker, M.R., Sudo, M., Stockli, D.F., Friedrich, A., Tabatabaei, S.H., 2011. Arabia-Eurasia continental collision: Insights from late Tertiary foreland-basin evolution in the Alborz Mountains, northern Iran. Geol. Soc. Am. Bull. 123 (1–2), 106–131. https://doi.org/10.1130/B30091.1.

Balázs, A., Faccenna, C., Ueda, K., Funiciello, F., Boutoux, A., Blanc, E.J.P., Gerya, T., 2021. Oblique subduction and mantle flow control on upper plate deformation: 3D geodynamic modeling. Earth Planet. Sci. Lett. 569, 117056. https://doi.org/10.1016/j.epsl.2021.117056.

Barber, D.E., Stockli, D.F., Horton, B.K., Koshnaw, R.I., 2018. Cenozoic exhumation and foreland basin evolution of the Zagros orogen during the Arabia-Eurasia collision, western Iran. Tectonics 37 (12), 4396–4420. https://doi.org/10.1029/2018TC005328.

Becker, T.W., Faccenna, C., 2011. Mantle conveyor beneath the Tethyan collisional belt. Earth Planet. Sci. Lett. 310, 453–461. https://doi.org/10.1016/j.epsl.2011.08.021.

Bird, 1979. Continental delamination and the Colorado Plateau. Journal of Geophysical Research: Solid Earth 84, B13, 7561-7571. Doi: 10.1029/JB084iB13p07561.

Boonma, K., García-Castellanos, D., Jiménez-Munt, I., Gerya, T., 2023. Thermomechanical modelling of lithospheric slab tearing and its topographic response. Front. Earth Sci. 11, 1095229. https://doi.org/10.3389/feart.2023.1095229.

Boutoux, A., Briaud, A., Faccenna, C., Ballato, P., Rossetti, F., Blanc, E., 2021. Slab folding and surface deformation of the Iran mobile belt e2020TC006300 Tectonics 40. https://doi.org/10.1029/2020TC006300.

Burov, E.B., 2011. Rheology and strength of the lithosphere. Mar. Pet. Geol. 28 (8), 1402–1443. https://doi.org/10.1016/j.marpetgeo.2011.05.008.

Chang, S.-J., Van der Lee, S., Flanagan, M.P., Bedle, H., Marone, F., Matzel, E.M., Pasyanos, M.E., Rodgers, A.J., Romanowicz, B., Schmid, C., 2010. Joint inversion for 3- dimensional S-velocity mantle structure along the Tethyan margin. J. Geophys. Res. Solid Earth 115, B08309. https://doi.org/10.1029/2009JB007204.

Chiu, H.-Y., Chung, S.-L., Zarrinkoub, M.H., Mohammadi, S.S., Khatib, M.M., Iizuka, Y., 2013. Zircon U-Pb age constraints from Iran on the magmatic evolution related to Neotethyan subduction and Zagros orogeny. Lithos 162–163, 70–87. https://doi.org/10.1016/j. lithos.2013.01.006.

Crameri, F., Schmeling, H., Golabek, G., Duretz, T., Orendt, R., Buiter, S., et al., 2012. A comparison of numerical surface topography calculations in geodynamic modelling: An evaluation of the 'sticky air' method. Geophys. J. Int. 189 (1), 38–54. https://doi.org/10.1111/j.1365-246X.2012.05388.x.

Darin, M.H., Umhoefer, P.J., 2022. Diachronous initiation of Arabia-Eurasia collision from eastern Anatolia to the southeastern Zagros Mountains since middle Eocene time. Int. Geol. Rev. 64 (18), 2653–2681. https://doi.org/10.1080/00206814.2022.2048272.

Dashti, F., Lucente, F.P., Motaghi, K., Bianchi, I., Najafi, M., Govoni, A., Shabanian, E., 2020. Crustal scale imaging of the Arabia-Central Iran collision boundary across the Zagros suture zone, west of Iran e2019GL085921 Geophys. Res. Lett. 47. https://doi.org/10.1029/2019GL085921.

Duretz, T., Gerya, T.V., May, D.A., 2011. Numerical modelling of spontaneous slab breakoff and subsequent topographic response. Tectonophysics 502 (1–2), 244–256. https://doi.org/10.1016/j.tecto.2010.05.024.

Dymkova, D., Gerya, T., Burg, J.-P., 2016. 2D thermomechanical modelling of continent–arc–continent collision. Gondw. Res. 32, 138–150. https://doi.org/10.1016/j.gr.2015.02.012.

Ershov, A.V., Nikishin, A.M., 2004. Recent geodynamics of the Caucasus-Arabia-east Africa region. Geotectonics 38 (2), 123–136.

Evans, B., Goetze, C., 1979. The temperature variation of hardness of olivine and its implication for polycrystalline yield stress. J. Geophys. Res. Solid Earth 84 (B10), 5505–5524. https://doi.org/10.1029/JB084iB10p05505.

Faccenda, M., Gerya, T.V., Chakraborty, S., 2008. Styles of post-subduction collisional orogeny: Influence of convergence velocity, crustal rheology and radiogenic heat production. Lithos 103 (1), 257–287. https://doi.org/10.1016/j.lithos.2007.09.009.

Faccenna, C., Becker, T.W., Jolivet, L., Keskin, M., 2013. Mantle convection in the Middle East: Reconciling Afar upwelling, Arabia indentation and Aegean trench rollback. Earth Planet. Sci. Lett. 375, 254–269. https://doi.org/10.1016/j.epsl.2013.05.043.

Gao, Y., Chen, L., Talebian, M., Wu, Z., Wang, X., et al., 2022. Nature and structural heterogeneities of the lithosphere control the continental deformation in the northeastern and eastern Iranian plateau as revealed by shear-wave splitting observations. Earth Planet. Sci. Lett. 578, 117284. https://doi.org/10.1016/j.epsl.2021.117284.

Gao, Y., Chen, L., Yang, J., Wang, K., 2023. Rheological heterogeneities control the non-progressive uplift of the young Iranian plateau e2022GL101829 Geophys. Res. Lett. 50. https://doi.org/10.1029/2022GL101829.

Gavillot, Y., Axen, G.J., Stockli, D.F., Horton, B.K., Fakhari, M.D., 2010. Timing of thrust activity in the High Zagros fold-thrust belt, Iran, from (U-Th)/He thermochronometry. Tectonics 29 (4). https://doi.org/10.1029/2009TC002484.

Gerya, T.V., Meilick, F.I., 2010. Geodynamic regimes of subduction under an active margin: effects of rheological weakening by fluids and melts. J. Metam. Geol. 29, 1. https://doi.org/10.1111/j.1525-1314.2010.00904.x.

Gerya, T.V., Yuen, D.A., 2003. Characteristics-based marker-in-cell method with conservative finite-differences schemes for modeling geological flows with strongly variable transport properties. Phys. Earth Planet. In. 140 (4), 293–318. https://doi.org/10.1016/j.pepi.2003.09.006.

Gerya, T.V., Stöckhert, B., Perchuk, A.L., 2002. Exhumation of high-pressure metamorphic rocks in a subduction channel: A numerical simulation. Tectonics 21 (6), 1056. https://doi.org/10.1029/2002TC001406.

Gerya, T.V., Connolly, J.A., Yuen, D.A., Gorczyk, W., Capel, A.M., 2006. Seismic implications of mantle wedge plumes. Phys. Earth Planet. In. 156 (1–2), 59–74. https://doi.org/10.1016/j.pepi.2006.02.005.

Gerya, T.V., Stern, R.J., Baes, M., Sobolev, S.V., Whattam, S.A., 2015. Plate tectonics on the Earth triggered by plume-induced subduction initiation. Nature 527, 221–225. https://doi.org/10.1038/nature15752.

Gerya, T., 2019. Introduction to numerical geodynamic modelling. Cambridge University Press, p. p. 471)..

Gorczyk, W., Willner, A.P., Gerya, T.V., Connolly, J.A., Burg, J.-P., 2007. Physical controls of magmatic productivity at Pacific-type convergent margins: Numerical modelling. Phys. Earth Planet. In. 163 (1), 209–232. https://doi.org/10.1016/j.pepi.2007.05.010.

Hacker, B.R., Kelemen, P.B., Behn, M.D., 2011. Differentiation of the continental crust by relamination. Earth Planet. Sci. Lett. 307 (3–4), 501–516. https://doi.org/10.1016/j.epsl.2011.05.024.

Hackney, R.I., Featherstone, W.E., 2003. Geodetic versus geophysical perspectives of the 'gravity anomaly'. Geophys. J. Int. 154 (1), 35–43. https://doi.org/10.1046/j.1365-246X.2003.01941.x.

Hinze, W.J., 2003. Bouguer reduction density, why 2.67? Geophysics 68 (5), 1559–1560. https://doi.org/10.1190/1.1620629.

Huismans, R.S., Beaumont, C., 2002. Asymmetric lithospheric extension: The role of frictional plastic strain softening inferred from numerical experiments. Geology 30 (3), 211–214. https://doi.org/10.1130/0091-7613(2002)030<0211:ALETRO>2.0.CO;2.

Irandoust, M.A., Priestley, K., Sobouti, F., 2022. High-resolution lithospheric structure of the Zagros collision zone and Iranian Plateau e2022JB025009 Journal of Geophysical Research: Solid Earth 127. https://doi.org/10.1029/2022JB025009.

Karato, S.-I., Wu, P., 1993. Rheology of the upper mantle: A synthesis. Science 260 (5109), 771–778. https://doi.org/10.1126/science.260.5109.771.

Katayama, I., Karato, S.-I., 2008. Low-temperature, high-stress deformation of olivine under water-saturated conditions. Phys. Earth Planet. In. 168 (3), 125–133. https://doi.org/10.1016/j.pepi.2008.05.019.

Kaviani, A., Sandvol, E., Moradi, A., Rümpker, G., Tang, Z., Mai, P.M., 2018. Mantle transition zone thickness beneath the Middle East: Evidence for segmented Tethyan slabs, delaminated lithosphere, and lower mantle upwelling. J. Geophys. Res. Solid Earth 123, 4886–4905. https://doi.org/10.1029/2018JB015627.

Kaviani, A., Paul, A., Moradi, A., Mai, P.M., Pilia, S., Boschi, L., et al., 2020. Crustal and uppermost mantle shear wave velocity structure beneath the Middle East from surface wave tomography. Geophys. J. Int. 221 (2), 1349–1365. https://doi.org/10.1093/gji/ ggaa075.

Khorrami, F., Vernant, P., Masson, F., Nilfouroushan, F., Mousavi, Z., Nankali, H., et al., 2019. An up-to-date crustal deformation map of Iran using integrated campaign-mode and permanent GPS velocities. Geophys. J. Int. 217 (2), 832–843. https://doi.org/10.1093/gji/ggz045.

Kirby, J.F., 2014. Estimation of the effective elastic thickness of the lithosphere using inverse spectral methods: the state of the art. Tectonophysics 631 (C), 87–116. https://doi.org/10.1016/j.tecto.2014.04.021.

Koptev, A.I., Ershov, A.V., 2011. Thermal thickness of the Earth's lithosphere: a numerical model. Mosc. Univ. Geol. Bull. 66, 323–330. https://doi.org/10.3103/S014587521105005X.

Koptev, A., Gerya, T., Calais, E., Leroy, S., Burov, E., 2018. Afar triple junction triggered by plume-assisted bi-directional continental break-up. Scientific Reports 8, 14742. https://doi.org/10.1038/s41598-018-33117-3.

Koptev, A., Ehlers, T.A., Nettesheim, M., Whipp, D.M., 2019. Response of a rheologically stratified lithosphere to subduction of an indenter-shaped plate: insights into localized exhumation at orogen syntaxes. Tectonics 38 (6), 1908–1930. https://doi.org/10.1029/2018TC005455.

Koptev, A., Cloetingh, S., Kovács, I.J., Gerya, T., Ehlers, T.A., 2021. Controls by rheological structure of the lithosphere on the temporal evolution of continental magmatism: inferences from the Pannonian Basin system. Earth Planet. Sci. Lett. 565, 116925. https://doi.org/10.1016/j.epsl.2021.116925.

Koptev, A., Nettesheim, M., Ehlers, T.A., 2022. Plate corner subduction and rapid localized exhumation: insights from 3D coupled geodynamic and geomorphological modelling. Terra Nova 34 (3), 210–223. https://doi.org/10.1111/ter.12581.

Koshnaw, R.I., Stockli, D.F., Schlunegger, F., 2019. Timing of the Arabia-Eurasia continental collision: evidence from detrital zircon U-Pb geochronology of the Red Bed Series strata of the northwest Zagros hinterland. Kurdistan Region of Iraq: Geology 47, 47–50. https://doi.org/10.1130/G45499.1.

Koulakov, I., 2011. High-frequency P and S velocity anomalies in the upper mantle beneath Asia from inversion of worldwide traveltime data. J. Geophys. Res. Solid Earth 116 (B4), 430. https://doi.org/10.1029/2010JB007938.

Kvas, A., Brockmann, J.M., Krauss, S., Schubert, T., Gruber, T., Meyer, U., Mayer-Gürr, T., Schuh, W.-D., Jäggi, A., Pail, R., 2021. GOCO06s – a satellite-only global gravity field model. Earth Syst. Sci. Data 13 (1), 99–118. https://doi.org/10.5194/essd-13-99-2021.

Labrousse, L., Duretz, T., Gerya, T., 2015. H_2O-fluid-saturated melting of subducted continental crust facilitates exhumation of ultrahigh-pressure rocks in continental subduction zones. Earth Planet. Sci. Lett. 428, 151–161. https://doi.org/10.1016/j.epsl.2015.06.016.

Lavecchia, A., Filippucci, M., Tallarico, A., Selvaggi, G., Cecere, G., Cloetingh, S., 2022. Role of crustal fluids and thermo-mechanical structure for lower crustal seismicity: the Gargano Promontory (southern Italy). Global Planet. Change 217, 103929. https://doi.org/10.1016/j.gloplacha.2022.103929.

Li, Z.H., Xu, Z., Gerya, T., Burg, J.P., 2013. Collision of continental corner from 3-D numerical modeling. Earth Planet. Sci. Lett. 380, 98–111. https://doi.org/10.1016/j.epsl.2013.08.034.

Li, C.-F., Lu, Y., Wang, J., 2017. A global reference model of Curie-point depths based on EMAG. Sci. Rep. 7, 45129. https://doi.org/10.1038/srep45129.

Liu, M.Q., Li, Z.H., Yang, S.H., 2017. Diapir versus along-channel ascent of crustal material during plate convergence: constrained by the thermal structure of Subduction Zones. J. Asian Earth Sci. Struct. Process. Subduct. Zones 145, 16–36. https://doi.org/10.1016/j.jseaes.2017.02.036.

Madanipour, S., Ehlers, T.A., Yassaghi, A., Enkelmann, E., 2017. Accelerated middle Miocene exhumation of the Talesh Mountains constrained by U-Th/He thermochronometry: evidence for the Arabia-Eurasia collision in the NW Iranian Plateau. Tectonics 36 (8), 1538–1561. https://doi.org/10.1002/2016TC004291.

Maddaloni, F., Tesauro, M., Gerya, T.V., Pastorutti, A., Braitenberg, C., Delvaux, D., Munch, J., 2022. Effects of multi-extensional tectonics in a cratonic area: 3D numerical modeling and implications for the Congo basin. Gondw. Res. 111, 298–324. https://doi.org/10.1016/j.gr.2022.09.002.

Mahmoodabadi, M., Yaminifard, F., Tatar, M., 2019. Upper-mantle velocity structure beneath the Zagros collision zone, Central Iran and Alborz from nonlinear teleseismic tomography. Geophys. J. Int. 218, 414–428. https://doi.org/10.1093/gji/ggz160.

Mahmoodabadi, M., Yaminifard, F., Tatar, M., Kaviani, A., 2020. Shear wave velocity structure of the upper-mantle beneath the northern Zagros collision zone revealed by nonlinear teleseismic tomography and Bayesian Monte-Carlo joint inversion of surface wave dispersion and teleseismic P-wave coda. Phys. Earth Planet. In. 300, 106444. https://doi.org/10.1016/j.pepi.2020.106444.

Maierová, P., Schulmann, K., Gerya, T., 2018. Relamination styles in collisional orogens. Tectonics 37, 224–250. https://doi.org/10.1002/2017TC004677.

Malatesta, C., Gerya, T., Crispini, L., Federico, L., Capponi, G., 2013. Oblique subduction modelling indicates along-trench tectonic transport of sediments. Nat. Commun. 4 (1), 2456. https://doi.org/10.1038/ncomms3456.

Malatesta, C., Gerya, T., Crispini, L., Federico, L., Capponi, G., 2016. Interplate deformation at early-stage oblique subduction: 3-D thermomechanical numerical modeling. Tectonics 35 (7), 1610–1625. https://doi.org/10.1002/2016TC004139.

Maurizio, G., Braitenberg, C., Sampietro, D., Capponi, M., 2023. A new lithospheric density and magnetic susceptibility model of Iran, starting from high-resolution seismic tomography e2023JB027383 J. Geophys. Res. Solid Earth 128 (12). https://doi.org/10.1029/2023JB027383.

Menant, A., Sternai, P., Jolivet, L., Guillou-Frottier, L., Gerya, T., 2016. 3D numerical modeling of mantle flow, crustal dynamics and magma genesis associated with slab roll-back and tearing: The eastern Mediterranean case. Earth Planet. Sci. Lett. 442, 93–107. https://doi.org/10.1016/j.epsl.2016.03.002.

Meurers, B., 2017. Chapter 2 - The Physical Meaning of Bouguer Anomalies—General Aspects Revisited. In: Understanding the Bouguer Anomaly. Ed. by R. Pašteka, J. Mikuška, and B. Meurers, pp. 13–30. isbn: 978-0-12-812913-5. Doi: 10.1016/B978-0-12-812913-5.00001-4.

Mohammadi, E., Sodoudi, F., Kind, R., Rezapour, M., 2013. Presence of a layered lithosphere beneath the Zagros collision zone. Tectonophysics 608, 366–375. https://doi.org/10.1016/j.tecto.2013.09.017.

Mohammadi, N., Rahimi, H., Gholami, A., Pachhai, S., Aoudia, A., 2022. Shear-wave velocity structure of upper mantle along the Zagros collision zone. Tectonophysics 837, 229444. https://doi.org/10.1016/j.tecto.2022.229444.

Molinaro, M., Zeyen, H., Laurencin, X., 2005. Lithospheric structure beneath the south-eastern Zagros Mountains, Iran: recent slab break-off? Terra Nova 17 (1), 1–6. https://doi.org/10.1111/j.1365-3121.2004.00575.x.

Motaghi, K., Tatar, M., Priestley, K., Tatar, M., Romanelli, M., Doglioni, C., Panza, G.F., 2015. The deep structure of the Iranian Plateau. Gondw. Res. 28, 407–418. https://doi.org/10.1016/j.gr.2014.04.009.

Motaghi, K., Shabanian, E., Tatar, M., Cuffaro, M., Doglioni, C., 2017. The south Zagros suture zone in teleseismic images. Tectonophysics 694, 292–301. https://doi.org/10.1016/j.tecto.2016.11.012.

Mouthereau, F., Lacombe, O., J., Vergés, 2012. Building the Zagros collisional orogen: Timing, strain distribution and the dynamics of Arabia/Eurasia plate convergence. Tectonophysics 532-535, 27–60, 10.1016/j.tecto.2012.01.022. Doi: 10.1016/j.tecto.2012.01.022.

Muttoni, G., Gaetani, M., Kent, D.V., Sciunnach, D., Angiolini, L., Berra, F., et al., 2009. Opening of the Neo-Tethys Ocean and the Pangea B to Pangea. A Transformation during the Permian. Geoarabia 14 (4), 17–48. https://doi.org/10.2113/geoarabia140417.

Nolet, G., 1990. Partitioned waveform inversion and two-dimensional structure under the Network of Autonomously Recording Seismographs. J. Geophys. Res. Solid Earth 95, 8499–8512. https://doi.org/10.1029/JB095iB06p08499.

Omrani, J., Agard, P., Whitechurch, H., Benoit, M., Prouteau, G., Jolivet, L., 2008. Arc-magmatism and subduction history beneath the Zagros Mountains, Iran: A new report of adakites and geodynamic consequences. Lithos 106 (3–4), 380–398. https://doi.org/10.1016/j. lithos.2008.09.008.

Paul, A., Kaviani, A., Hatzfeld, D., Vergne, J., Mokhtari, M., 2006. Seismological evidence for crustal-scale thrusting in the Zagros mountain belt (Iran). Geophys. J. Int. 166, 227–237. https://doi.org/10.1111/j.1365-246X.2006.02920.x.

Paul, A., Hatzfeld, D., Kaviani, A., Tatar, M., Pequegnat, C., 2010. Seismic imaging of the lithospheric structure of the Zagros mountain belt (Iran). Geol. Soc. Lond. Spec. Publ. 330 (1), 5–18. https://doi.org/10.1144/SP330.2.

Perron, P., Guiraud, M., Vennin, E., Moretti, I., Portier, E., Le Pourhiet, L., Konaté, M., 2018. Influence of basement heterogeneity on the architecture of low subsidence rate Paleozoic intracratonic basins (Reggane, Ahnet, Mouydir and Illizi basins, Hoggar Massif). Solid Earth 9 (6), 1239–1275. Doi: 10.5194/se-9-1239- 2018.

Pivetta, T., Braitenberg, C., 2020. Sensitivity of gravity and topography regressions to earth and planetary structures. Tectonophysics 774, 228299. https://doi.org/10.1016/j.tecto.2019.228299.

Pons, M., Sobolev, S.V., Liu, S., Neuharth, D., 2022. Hindered trench migration due to slab steepening controls the formation of the Central Andes. J. Geophys. Res. Solid Earth e2022JB025229. https://doi.org/10.1029/2022JB025229.

Putirka, K.D., Perfit, M., Ryerson, F.J., Jackson, M.G., 2007. Ambient and excess mantle temperatures, olivine thermometry, and active vs. passive upwelling. Chem. Geol. 241 (3–4), 177–206. https://doi.org/10.1016/j.chemgeo.2007.01.014.

Rabiee, A., Rossetti, F., Tecce, F., Asahara, Y., Azizi, H., Glodny, J., Lucci, F., Nozaem, R., Opitz, J., Selby, D., 2019. Multiphase magma intrusion, ore-enhancement and hydrothermal carbonatisation in the Siah-Kamar porphyry Mo deposit, Urumieh-Dokhtar magmatic zone, NW Iran. Ore Geol. Rev. 110, 102930.

Rabiee, A., Rossetti, F., Asahara, Y., Azizi, H., Lucci, F., Lustrino, M., Nozaem, R., 2020. Long-lived, Eocene-Miocene stationary magmatism in NW Iran along a transform plate boundary. Gondw. Res. 85, 237–262. https://doi.org/10.1016/j.gr.2020.03.014.

Rabiee, A., Rossetti, F., Lucci, F., Lustrino, M., 2022. Cenozoic porphyry and other hydrothermal ore deposits along the South Caucasus-West Iranian tectono-magmatic belt: a critical reappraisal of the controlling factors. Lithos 430–431, 106874. https://doi.org/10.1016/j.lithos.2022.106874.

Rahmani, M., Motaghi, K., Ghods, A., Sobouti, F., Talebian, M., Ai, Y., et al., 2019. Deep velocity image of the north Zagros collision zone (Iran) from regional and teleseismic tomography. Geophys. J. Int. 219 (3), 1729–1740. https://doi.org/10.1093/gji/ggz393.

Ranalli, G., 1995. Rheology of the Earth: Springer Science & Business Media. 414pp. ISBN: 0412546701, 9780412546709.

Rashidi, A., Shahpasandzadeh, M., Braitenberg, C., 2022. Late cenozoic to present kinematic of the north to eastern iran orogen: accommodating opposite sense of fault blocks rotation. Remote Sens. (Basel) 14 (16), 4048. https://doi.org/10.3390/rs14164048.

Rashidi, A., Nemati, M., Shafieibafti, S., Pourbeyranvand, S., Derakhshani, R., Braitenberg, C., 2023. Structure and kinematics of active faulting in the northern domain of Western and Central Alborz, Iran and interpretation in terms of tectonic evolution of the region. J. Asian Earth Sci. 255, 105760. https://doi.org/10.1016/j.jseaes.2023.105760.

Rexer, M., Hirt, C., Claessens, S., Tenzer, R., 2016. Layer-based modelling of the Earth's gravitational potential up to 10-km scale in spherical harmonics in spherical and ellipsoidal approximation. Surv. Geophys. 37 (6), 1035–1074. https://doi.org/10.1007/s10712-016-9382-2.

Schaeffer, A.J., Lebedev, S., 2013. Global shear-speed structure of the upper mantle and transition zone. Geophys. J. Int. 194 (1), 417–449. https://doi.org/10.1093/gji/ggt095.

Schliffke, N., van Hunen, J., Magni, V., Allen, M.B., 2019. The role of crustal buoyancy in the generation and emplacement of magmatism during continental collision. Geochem. Geophys. Geosyst. 20 (11), 4693–4709. https://doi.org/10.1029/2019GC008590.

Schmeling, H., Babeyko, A., Enns, A., Faccenna, C., Funiciello, F., Gerya, T., et al., 2008. A benchmark comparison of spontaneous subduction models—towards a free surface. Phys. Earth Planet. In. 171 (1), 198–223. https://doi.org/10.1016/j.pepi.2008.06.028.

Sheng, J., Liao, J., Gerya, T., 2016. Numerical modeling of deep oceanic slab dehydration: Implications for the possible origin of far field intra-continental volcanoes in northeastern China. J. Asian Earth Sci. 117, 328–336. https://doi.org/10.1016/j.jseaes.2015.12.022.

Sibuet, J.C., Rouzo, S., Srivastava, S., 2012. Plate tectonic reconstructions and paleogeographic maps of the central and North Atlantic oceans. Can. J. Earth Sci. 49 (12), 1395–1415. https://doi.org/10.1139/e2012-071.

Simmons, N.A., Myers, S.C., Johannesson, G., 2011. Global-scale P wave tomography optimized for prediction of teleseismic and regional travel times for Middle East events: 2. Tomographic inversion. J. Geophys. Res. Solid Earth 116, B04305. https://doi.org/10.1029/2010JB007969.

Sizova, E., Gerya, T., Brown, M., 2012. Exhumation mechanisms of melt-bearing ultrahigh pressure crustal rocks during collision of spontaneously moving plates. J. Metam. Geol. 30 (9), 927–955. https://doi.org/10.1111/j.1525-1314.2012.01004.x.

Sleep, N.H., 2003. Geodynamic implications of xenolith geotherms. Geochem. Geophys. Geosyst. 4 (9), 1079. https://doi.org/10.1029/2003GC000511.

Stern, R.J., Gerya, T., 2018. Subduction initiation in nature and models: a review. Tectonophysics 746, 173–198. https://doi.org/10.1016/j.tecto.2017.10.014.

Sternai, P., Jolivet, L., Menant, A., Gerya, T., 2014. Driving the upper plate surface deformation by slab rollback and mantle flow. Earth Planet. Sci. Lett. 405, 110–118. https://doi.org/10.1016/j.epsl.2014.08.023.

Talebi A., Koulakov, I., Moradi, A., Rahimi, H., Gerya, T., 2020. Ongoing formation of felsic lower crustal channel by relamination in Zagros collision zone revealed from regional tomography. Scientific Report 10:8224 | Doi: 10.1038/s41598-020-64946-w.

Turcotte, D.L. and Schubert, G., 2002. *Geodynamics*. Cambridge Univ. Press, 863pp. http://dx.doi.org/10.1017/CBO9780511807442.

Ueda, K., Gerya, T.V., Burg, J.P., 2012. Delamination in collisional orogens: thermomechanical modeling. J. Geophys. Res. Solid Earth 117 (B8), B08202. https://doi.org/10.1029/2012JB009144.

Uieda, L., Barbosa, V., Braitenberg, C., 2016. Tesseroids: forward-modeling gravitational fields in spherical coordinates. Geophysics, F41–F48. https://doi.org/10.1190/geo2015-0204.1.

Vajda, P., Ellmann, A., Meurers, B., Vaníček, P., Novák, P., Tenzer, R., 2008. Global ellipsoid-referenced topographic, bathymetric and stripping corrections to gravity disturbance. Stud. Geophys. Geod. 52 (1), 19–34. https://doi.org/10.1007/s11200-008-0003-5.

Veisi, M., Sobouti, F., Chevrot, S., Abbasi, M., Shabanian, E., 2021. Upper mantle structure under the Zagros collision zone; insights from 3D teleseismic P-wave tomography. Tectonophysics 819, 229106. https://doi.org/10.1016/j.tecto.2021.229106.

Verdel, C., Wernicke, B.P., Hassanzadeh, J., Guest, B., 2011. A Paleogene extensional arc flare-up in Iran. Tectonics 30, TC3008. https://doi.org/10.1029/2010TC002809.

Vergés, J., Goodazari, M.H., Emami, H., Karpuz, R., Efstatiou, J., Gillespie, P., 2011. Multiple detachment folding in Pusht-e Kuh Arc, Zagros. Role of mechanical stratigraphy. In: McClay, K., Shaw, J., Suppe, J. (Eds.), Thrust Fault Related Folding. American Association of Petroleum Geologists Memoir 94, 1–26. DOI:10.1306/13251333M942899.

Vergés, J., Emami, H., Garcés, M., Beamud, E., Homke, S., Skott, P., 2019. Zagros foreland fold belt timing across Lurestan to constrain Arabia-Iran collision. Developments in Structural Geology and Tectonics, Vol. 3. Elsevier, pp. 29–52.

Vernant, P., Nilforoushan, F., Hatzfeld, D., Abbassi, M.R., Vigny, C., Masson, F., et al., 2004. Present-day crustal deformation and plate kinematics in the Middle East constrained by GPS measurements in Iran and northern Oman. Geophys. J. Int. 157 (1), 381–398. https://doi.org/10.1111/j.1365-246X.2004.02222.x.

Vogt, K., Gerya, T.V., Castro, A., 2012. Crustal growth at active continental margins: numerical modeling. Phys. Earth Planet. In. 192, 1–20. https://doi.org/10.1016/j.pepi.2011.12.003.

Vogt, K., Castro, A., Gerya, T., 2013. Numerical modeling of geochemical variations caused by crustal relamination. Geochem. Geophys. Geosyst. 14 (2), 470–487. https://doi.org/10.1002/ggge.20072.

Wilmsen, M., Fürsich, F.T., Seyed-Emami, K., Majidifard, M.R., Taheri, J., 2009. The Cimmerian Orogeny in northern Iran: Tectono-stratigraphic evidence from the foreland. Terra Nova 21 (3), 211–218. https://doi.org/10.1111/j.1365-3121.2009.00876.x.

Wu, Z., Chen, L., Talebian, M., Wang, X., Jiang, M., Ai, Y., et al., 2021. Lateral structural variation of the lithosphere-asthenosphere system in the northeastern to eastern Iranian Plateau and its tectonic implications e2020JB020256 J. Geophys. Res.: Solid Earth 126 (1). https://doi.org/10.1029/2020jb020256.

Yang, G., Chen, L., Zhao, L.-F., Xie, X.-B., Yao, Z.-X., 2023a. Crustal Lg attenuation beneath the Iranian Plateau: implications for Cenozoic magmatism related to slab subduction, slab break-off, and mantle flow e2022JB025664 J. Geophys. Res. Solid Earth 128. https://doi.org/10.1029/2022JB025664.

Yang, G., Chen, L., Zhao, L.-F., Xie, X.-B., Yao, Z.-X., 2023b. Segmented up-bending of the Arabian continental plate revealed by Pn attenuation tomography e2023JB028062 J. Geophys. Res. Solid Earth 128. https://doi.org/10.1029/2023JB028062.

Zanchi, A., Zanchetta, S., Berra, F., Mattei, M., Garzanti, E., Molyneux, S., et al., 2009. The Eo-Cimmerian (Late? Triassic) orogeny in North Iran. Geol. Soc. Lond. Spec. Publ. 312 (1), 31–55. https://doi.org/10.1144/SP312.3.

Zingerle, P., Pail, R., Gruber, T., Oikonomidou, X., 2020. The combined global gravity field model XGM2019e. J. Geod. 94 (7), 66. https://doi.org/10.1007/s00190-020-01398-0.